Challenge Journal of
STRUCTURAL MECHANICS

Vol.9 No.4 (2023)

auxetic building codes compressive strength dynamic analysis earthquake finite element analysis finite element method girder bridge mechanical properties metaheuristic algorithms modal analysis optimization prestresing pushover analysis reinforced concrete seismic design shallow foundations smart concrete steel structures structural dynamics temperature effects thick plate wind

TULPAR
ACADEMIC PUBLISHING

ISSN 2149-8024

EDITOR-IN-CHIEF

Assoc. Prof. Dr. Fatih Mehmet ÖZKAL
Atatürk University, Türkiye

CO-EDITOR-IN-CHIEF

Prof. Dr. Serdar ÇARBAŞ
Karamanoğlu Mehmetbey University, Türkiye

EDITORIAL BOARD

Prof. Dr. A. Ghani RAZAQPUR
McMaster University, Canada

Prof. Dr. Paulo B. LOURENÇO
University of Minho, Portugal

Prof. Dr. Gilbert Rainer GILLICH
Eftimie Murgu University of Resita, Romania

Prof. Dr. Long-Yuan LI
University of Plymouth, United Kingdom

Prof. Dr. Željana NIKOLIĆ
University of Split, Croatia

Prof. Dr. Habib UYSAL
Atatürk University, Türkiye

Prof. Dr. Filiz PİROĞLU
İstanbul Technical University, Türkiye

Prof. Dr. Alper BÜYÜKKARAGÖZ
Gazi University, Türkiye

Prof. Dr. Oğuz Akın DÜZGÜN
Atatürk University, Türkiye

Assoc. Prof. Dr. Bing QU
California Polytechnic State University, United States

Assoc. Prof. Dr. Naida ADEMOVIĆ
University of Sarajevo, Bosnia and Herzegovina

Prof. Dr. Halil SEZEN
The Ohio State University, United States

Prof. Dr. Adem DOĞANGÜN
Uludağ University, Türkiye

Prof. Dr. M. Asghar BHATTI
University of Iowa, United States

Prof. Dr. Reza KIANOUSH
Ryerson University, Canada

Prof. Dr. Y. Cengiz TOKLU
Beykent University, Türkiye

Prof. Dr. Togay ÖZBAKKALOĞLU
Texas State University, United States

Prof. Dr. Mehmet ÖZYAZICIOĞLU
Atatürk University, Türkiye

Prof. Dr. Hélio Luiz SIMONETTI
Federal Institute of Minas Gerais, Brazil

Assoc. Prof. Dr. Khaled MARAR
Eastern Mediterranean University, Cyprus

Assoc. Prof. Dr. Hong SHEN
Shanghai Jiao Tong University, China

Assoc. Prof. Dr. Nunziante VALOROSO
Parthenope University of Naples, Italy

Assoc. Prof. Dr. Anna SAETTA
IUAV University of Venice, Italy

Assoc. Prof. Dr. Amin GHANNADIASL
University of Mohaghegh Ardabili, Iran

Dr. Zühal ÖZDEMİR
The University of Sheffield, United Kingdom

Dr. Syahril TAUFIK
Lambung Mangkurat University, Indonesia

Dr. J. Michael GRAYSON
The Citadel - The Military College of South Carolina, United States

Dr. Fabio MAZZA
University of Calabria, Italy

Dr. Alberto Maria AVOSSA
Second University of Naples, Italy

Dr. Susanta GHOSH
Michigan Technological University, United States

Dr. Burak Kaan ÇIRPICI
Erzurum Technical University, Türkiye

Dr. Panatchai CHETCHOTISAK
Rajamangala University of Technology Isan, Thailand

Dr. Chitaranjan PANY
Vikram Sarabhai Space Centre, India

Dr. Ehsan HARIRCHIAN
Bauhaus-Universität Weimar, Germany

Assoc. Prof. Dr. Taha IBRAHIM
Benha University, Egypt

Dr. Sandro CARBONARI
Marche Polytechnic University, Italy

Dr. Chien-Kuo CHIU
National Taiwan University of Science and Technology, Taiwan

Dr. Teng WU
University at Buffalo, United States

Dr. Pierfrancesco CACCIOLA
University of Brighton, United Kingdom

Dr. Marco CORRADI
University of Perugia, Italy

Dr. José SANTOS
University of Madeira, Portugal

Dr. Luca LANDI
University of Bologna, Italy

Dr. Mirko MAZZA
University of Calabria, Italy

Dr. Süleyman Nazif ORHAN
Erzurum Technical University, Türkiye

Dr. Casim YAZICI
Ağrı İbrahim Çeçen University, Türkiye

E-mail: *cjsmec@challengejournal.com*

Web page: *cjsmec.challengejournal.com*

TULPAR Academic Publishing
www.tulparpublishing.com

Challenge Journal of Structural Mechanics

CONTENTS

Research Articles

TULPAR
ACADEMIC PUBLISHING

CHALLENGE JOURNAL OF STRUCTURAL MECHANICS 9 (4) (2023) 125–132

Research Article

Investigation of optimum tuned mass damper parameter according to stroke capacity

Aylin Ece Kayabekir [a]

[a] *Department of Civil Engineering, İstanbul Gelişim University, 34310 İstanbul, Türkiye*

ABSTRACT

During major earthquakes, civil structures may collapse due to vibration that has a frequency close to the frequency content of the structure. Because of this, control systems have also been proposed for building structures. These systems can be active ones that are controlled by electronic devices or passive ones that are tuned mechanical systems. Passive tuned mass dampers (TMDs) include mass, stiffness element and damping element and these are tuned around the frequency of the structure. For optimum tuning and the complex nature of the mathematics under random vibrations, metaheuristic algorithms are needed to be used. In the presented study, TMDs are optimized via Jaya algorithm. The control system was optimized for displacement minimization of the structure. Additionally, the stroke amount of the system was limited. The stroke capacity factor was investigated for wide limits between 0.5 and 4 for normalized stroke according to the maximum displacement of the structure. The investigation was done for a single degree of freedom structure for a general conclusion. It is observed that the stroke limit did not affect performance and optimum parameters after 2.75. The small values of the stroke limit have significantly different optimum period.

ARTICLE INFO

Article history:
Received 23 June 2023
Revised 11 August 2023
Accepted 14 September 2023

Keywords:
Tuned mass damper
Stroke
Control
Jaya algorithm
Vibration
Earthquake

1. Introduction

Numerous control systems have been developed to mitigate the dynamic effects caused by undesirable external factors. Advances in technology and computing have made the implementation of these systems more accessible, and they are widely employed in various mechanical systems, including structures.

In modern cities, buildings have been constructed taller to accommodate growing populations, and long bridges facilitate transportation. Given various factors, notably earthquakes, control systems have become essential for these structures. Merely ensuring safety and reliability is insufficient; these buildings must withstand minimal vibration during earthquakes and strong winds.

In general, two main types of control systems exist: active and passive. Active control systems use an external power source to exert force on the building, either augmenting or dissipating energy within the structure. Active feedback control systems transmit the system's response, measured by physical sensors, as a signal to the control actuator. These systems regulate responses affected by both internal and external influences, with a focus on safety and comfort.

On the other hand, passive control systems do not rely on an external power source but utilize mechanical forces. The effectiveness of passive control depends on the building's design and incorporation of viscoelastic materials to achieve optimal efficiency. Passive systems are more widely used and can be added to existing structures.

Additionally, semi-active and hybrid systems are also present. Passive-tuned mass dampers, composed of mass, spring-like stiffness elements, and viscous dampers, take the form of pendulums or series of isolation systems. Viscoelastic dampers convert kinetic energy into heat energy, effectively damping wind-induced loads in multi-story buildings since the 1980s.

---

* *Corresponding author*. Tel.: +90-212-422-7000 ; E-mail address: aekayabekir@gelisim.edu.tr (A. E. Kayabekir)

ISSN: 2149-8024 / DOI: https://doi.org/10.20528/cjsmec.2023.04.001

Tuned mass dampers have been successfully applied in various structures since 1971, such as the Citicorp Center, John Hancock Tower, and Fukuoka Tower. Taipei 101 boasts a remarkable example of a mass damper, the tallest and heaviest worldwide, weighing 730 tons and spanning five floors.

Throughout history, numerous advancements have been made in the field of tuned mass dampers (TMDs) to address the dynamic effects caused by external factors. The foundations of TMDs were laid by Herman Frahm in 1909 when he invented a device to prevent vibrations in ship machinery. His subsequent study on vibration control served as the basis for TMDs. By 1911, Frahm (1909) obtained a patent for his invention, which he called a tuned vibration damper. In 1928, Ormondroyd and Den Hartog initiated theoretical studies on modulated mass dampers. Den Hartog's work in 1949 led to a system where the mass lacked natural damping. However, later studies revealed that TMDs with damping are more effective due to enhanced energy conversion. Over the years, researchers like Bishop and Welbourn (1952) and Hartog (1956) further contributed to TMD research, exploring the damping parameters and optimizing their efficiency under different excitation conditions. From 1971 onwards, TMDs started being applied in various structures, with researchers continuously seeking to enhance their performance. Studies by Falcon et al. (1967), Ioi and Ikeda (1978), and Warburton and Ayorinde (1980) proposed methods to optimize TMD parameters. Subsequent research by various authors, including Xu and Igusa (1992), Tsai and Lin (1993), and Villaverde and Koyoama (1993), delved into optimizing TMD design for different types of structures and excitations. In the 21st century, researchers explored novel concepts, such as tuned mass damper-inerter (TMDI) devices (Marian and Giaralis 2014) and variable-tuned mass damping inerter (VTMDI) models (Li et al., 2020), to improve TMD performance and adaptability. In recent years, efforts have been made to optimize TMDs' performance in different scenarios, considering nonlinear behavior (Domenico and Ricciardi 2018) and integrating electromechanical components for energy conversion (Petrini et al. 2020). Advanced metaheuristic techniques like particle swarm optimization (PSO) (Leung and Zhang, 2009), harmony search, bat algorithm (Bekdaş and Nigdeli 2017) and genetic algorithms (Frans and Arfiadi 2015) have been applied to optimize TMD design.

Zucca et al. (2021) proposed a methodology for the TMD-controlled design of a historic masonry chimney, including a two-step optimization procedure. Caicedo et al (2021) developed a differential evolution method based optimization process for tuned mass dampers (TMDs) and tuned mass dampers inerter (TMDIs) placed on the upper floors of high-rise buildings exposed to seismic effects. Ant colony optimization was employed by Soheili et al. (2021) in order to minimize of the story drifts of a 40-story building considering soil structure interaction. Yücel et al (2022) introduced flower pollination algorithm for the reduction of critical displacements in the time-history domain Different TMD configurations including single and multiple TMD attached to nonlinear structures was optimized by Domizio et al. (2022) via PSO to increase effectiveness of seismic response control. Araz et al. (2023) investigated the optimum TMD design for a high-rise building to reduce the structural response under various embedment depths and soil properties. Mohsen Khatibinia et al. (2023) proposed an approach based on passive ensemble particle swarm and gray wolf optimization techniques in order to design optimum TMDs by considering seismic damage representing structural responses.

The optimum design parameters for tuned mass dampers must be also suitable for practical applications. For that reason, the stroke capacity of TMD must be considered in the optimum design which includes optimization of period and damping ratio of TMD for minimization of structural displacement. The stroke capacity was included as a design constraint by Bekdaş and Nigdeli 2017) using harmony search and bat algorithm. In the present study, stroke factor was investigated for a wide range that have maximum limit ($st_{\max}$) between 0.5 and 4.0 for normalized stroke. The normalized stroke is the ratio of drift of TMD and maximum displacement of the structure without TMD. Jaya algorithm that is developed by Rao (2016) was used in the methodology since it is a parameter free algorithm.

2. Methodology

In this study, software has been developed that analyzes the tuned mass dampers placed on a single degree of freedom system. The equation of motion of damped free vibration of structural systems under dynamic effects is given below.

$$\boldsymbol{M}\ddot{x}(t)+\boldsymbol{C}\dot{x}(t)+\boldsymbol{K}x(t)=-\boldsymbol{M}\{\boldsymbol{1}\}\ddot{x}_g(t) \tag{1}$$

The Matlab Simulink block diagram that provides the solution of this Eq. (1) for the developed software is given in Fig. 1.

In Eq. (1), *x* is the displacement vector. The equivalent of *x* in the block diagram is expressed as *Y*. Each point on the *x* vector has its derivative, the first derivative corresponds to velocity and the second derivative to acceleration. The equivalent of these values in the block diagram are defined as *Y*1 and *Y*2, respectively. In the diagram, E is the earthquake record, Etime corresponds to the earthquake time vector with 0.005 steps, and Y3 is earthquake acceleration ($\ddot{x}_g(t)$). In the equation of motion, M, C, K are mass, damping and stiffness matrices, respectively, given in Eqs. (2-4). In the block diagram, these matrices are seen as Mmatrix, Cmatrix and Kmatrix.

$$\boldsymbol{M}=\begin{bmatrix} m & \\ & m_d \end{bmatrix} \tag{2}$$

$$\boldsymbol{K}=\begin{bmatrix} k+k_d & -k_d \\ k_d & k_d \end{bmatrix} \tag{3}$$

$$\boldsymbol{C}=\begin{bmatrix} c+c_d & -c_d \\ c_d & c_d \end{bmatrix} \tag{4}$$

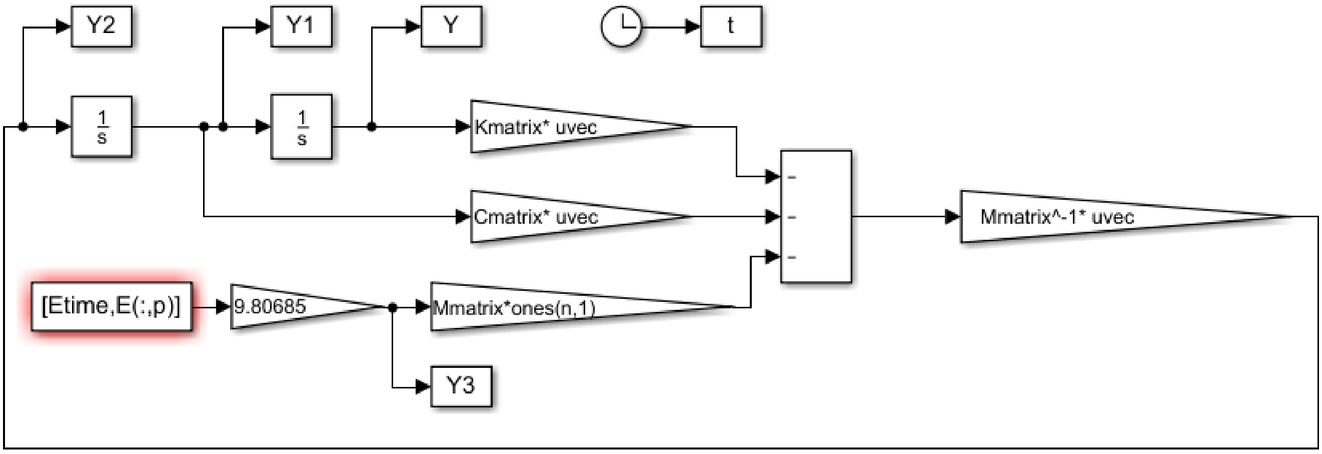

Fig. 1. The Matlab Simulink block diagram for dynamic analysis.

In the equations, *m*, *c*, *k* are the mass, damping and rigidity of the structure, respectively. Values with *d* subscript are the parameters used for TMD.

Dynamic analyzes were made under a total of 44 different earthquake records, 22 earthquakes and bidirectional ones given in FEMA P-695 as far-fault ground motions. The aim is to apply all earthquake records of the building in the design and to consider even the most unfavorable situation in terms of structural reactions under these records. What is meant by the most favorable situation is the analysis of the earthquake that causes the greatest displacement in the structure. This earthquake is defined as a critical earthquake in the study.

In order to apply the effects of these 44 earthquakes and compare their structural responses, the time step interval of the earthquake record is arranged equally. The Simulink block diagram that performs this editing process in the code is presented in Fig. 2.

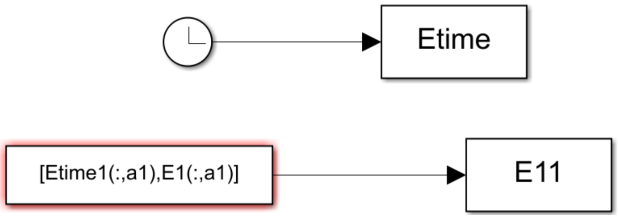

Fig. 2. The Matlab Simulink block diagram for earthquake data.

In the analysis process, the best combination of TMD parameters (m_d, c_d and k_d) for the structure is investigated. The definition of the best combination refers to the parameters that give the lowest displacement (x) under the dynamic effects of the structure. In the search process, Jaya algorithm, one of the metaheuristic algorithms, was used.

The optimization process with metaheuristic algorithms can be summarized in 3 stages, namely pre-optimization, analysis and optimization stage. In the pre optimization step, the problem is defined via entering data of earthquake records, design constants, limit values of design variables and population (solution vector) number. There are 4 design constants for the problem. These are the mass of the structure, the stiffness coefficient and damping ratio, and the TMD stroke limit ($st_{\max}$). TMD optimization was done for constant mass ratio that 5%. The design variable of TMD that are optimized are period (T_d) (as seen in Eq. (5)), and damping ratio (ξ_d) (as seen in Eq. (6)). Then an initial solution matrix including candidate solution vectors as much as population number is generated. A candidate solution vector consists of randomly generated values within ultimate limits of each design variables.

$$T_d = 2\pi\sqrt{\frac{m_d}{k_d}} \tag{5}$$

$$\xi_d = \frac{c_d}{2m_d\sqrt{\frac{k_d}{m_d}}} \tag{6}$$

In the analysis stage, the objective function is calculated and the design constraints are checked. The goal of optimization is to find the TMD design that provide the minimum displacement. Accordingly, the objective function is defined as follows.

$$f(x) = \text{minimize}(|x|) \tag{7}$$

As the design constraint the normalized stroke must be lower or equal to stroke limit ($st_{\max}$) as given in Eq. (8).

$$\frac{\max[|x_d - x|]_{\text{with}TMD}}{\max[|x|]_{\text{without}TMD}} \leq st_{\max} \tag{8}$$

In the last stage, using the existing solutions (X_{old}) stored in the initial solution matrix new solutions (X_{new}) are generated according to the algorithm equations. Algorithm have one equation as follow.

$$X_{\text{new}} = X_{\text{old}} + \text{rand} \cdot (g^{*} - |X_{\text{old}}|) - \text{rand} \cdot (g^{w} - |X_{\text{old}}|) \quad (9)$$

where g^{*} and g^{w} are best and worst solutions respectively. “rand” is a function that produce random values between 0 and 1.

The pseudocode of the search process performed as iterative is shown below. The stages of methodology are given in Table 1.

Table 1. Methodology stages

An example of stages in metaheuristic-based optimization
Data entering stage
Initial stage:
Generation of initial solution with random design variables
Structural analyses without TMD
Structural analyses with TMD
Iterative stage begins
New solution generation stage
Structural analysis with TMD
Selection and elimination stage
Save and output results

3. Numerical Examples

The numerical example includes a single degree of freedom structure that has 1 s period and 5% inherent damping. In optimization, the period limits of TMD are taken between 0.5s and 1.5s. The damping ratio of TMD was searched between 0.01 and 0.5. All optimum results and the objective function which is the maximum displacement of TMD are given in Table 2.

Table 2. Results of design variables for different stroke capacity

$st_{\max}$	T_d (s)	ξ_d	X (m)
0.50	0.694	0.500	0.272
0.75	0.894	0.500	0.265
1.00	0.907	0.351	0.258
1.25	0.902	0.246	0.252
1.50	0.932	0.196	0.247
1.75	0.912	0.131	0.242
2.00	0.910	0.088	0.237
2.25	0.943	0.080	0.233
2.50	0.955	0.065	0.231
2.75	0.948	0.047	0.231
3.00	0.944	0.033	0.230
3.25	0.941	0.023	0.229
3.50	0.939	0.014	0.228
3.75	0.938	0.010	0.228
4.00	0.938	0.010	0.228

As seen in Fig. 3, the optimum period remains the same after 2.75 stroke limit. By the decrease of TMD mobility, the optimum period decreases. All optimum periods are below the natural period of the structure.

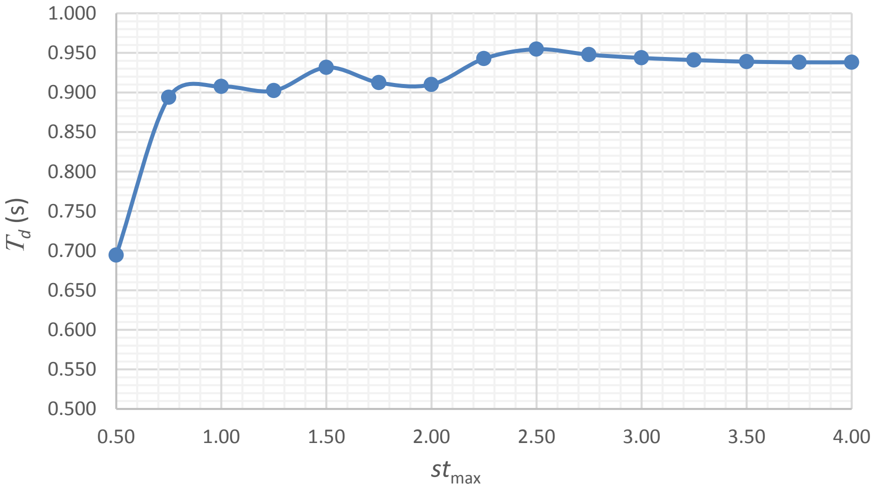

Fig. 3. Relationship of period according to $st_{\max}$.

According to Fig. 4, the optimum damping ratio is at the maximum limit for $st_{\max}$ 0.75 and 0.5 values. If the stroke limit is very big, damping is not important in optimum design.

As seen in Fig. 5, the maximum displacement is highly reduced up to 2.5 stroke limit, but there are no critical change if the stroke limit is higher than 2.5.

Time history graphs were also drawn for the 4 cases ($st_{\max}$ 0.5, 1, 2 and 3 cases) selected as examples to demonstrate the performance of TMD on structural displacement. Component1 of Imperial Valley (IMPVALL/H-E11140) earthquake record is a critical earthquake for all cases. Time history graphs for this earthquake are presented in Figs. 6- 9 for different $st_{\max}$ cases in comparison with TMD.

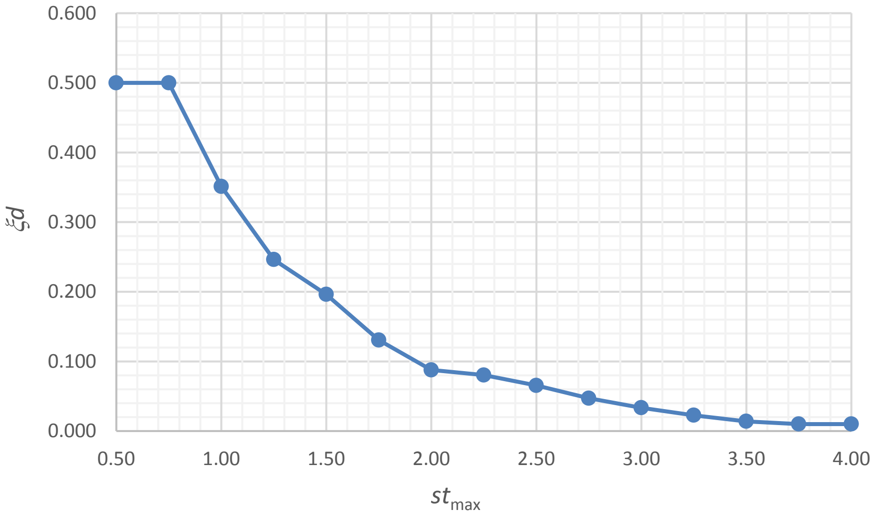

Fig. 4. Relationship of damping ratio according to st_{max}.

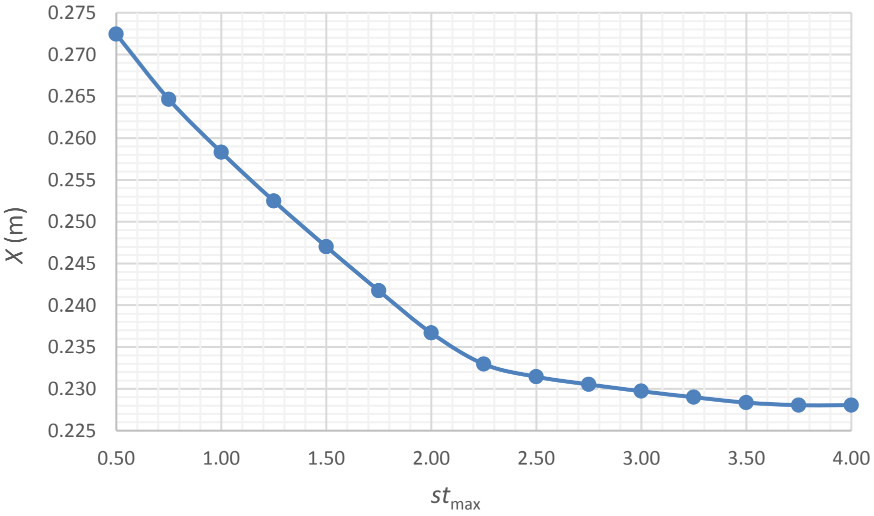

Fig. 5. Relationship of displacement according to st_{max}.

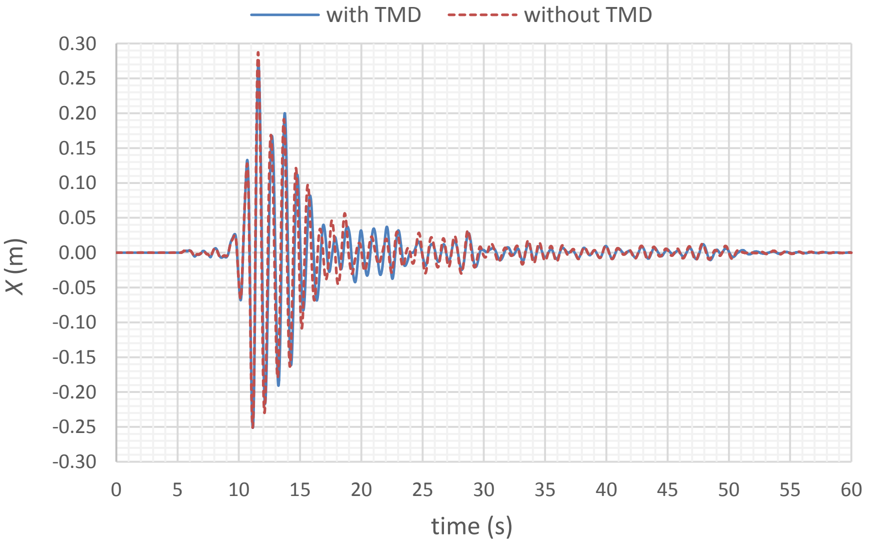

Fig. 6. Time History plots with TMD (st_{max}=0.5) and without TMD cases.

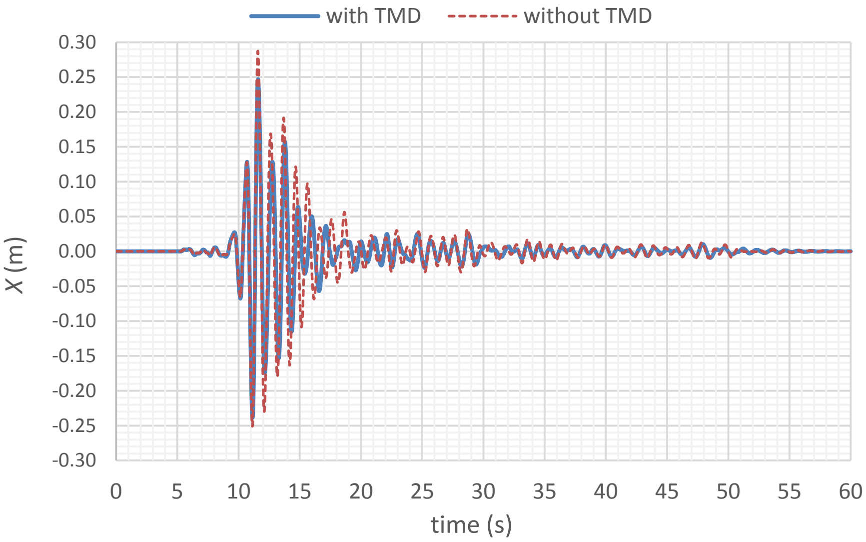

Fig. 7. Time History plots with TMD ($st_{\max}$=1.5) and without TMD cases.

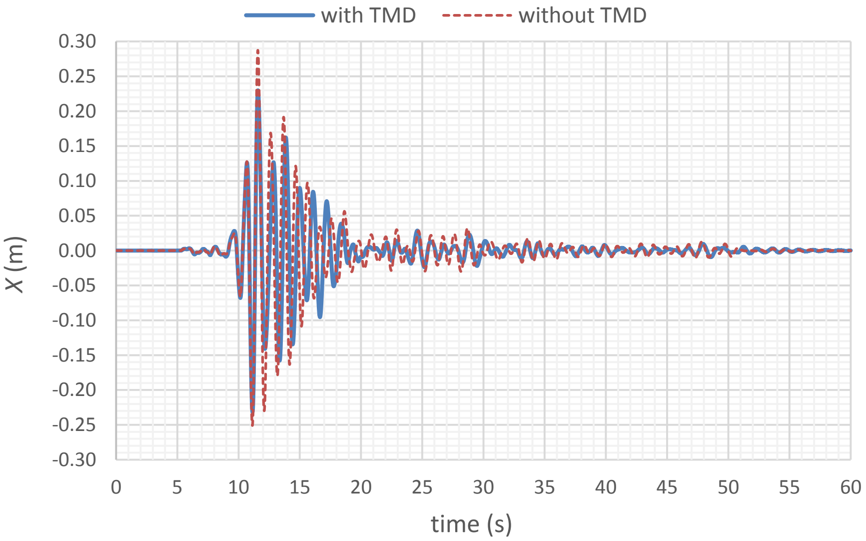

Fig. 8. Time History plots with TMD ($st_{\max}$=2.5) and without TMD cases.

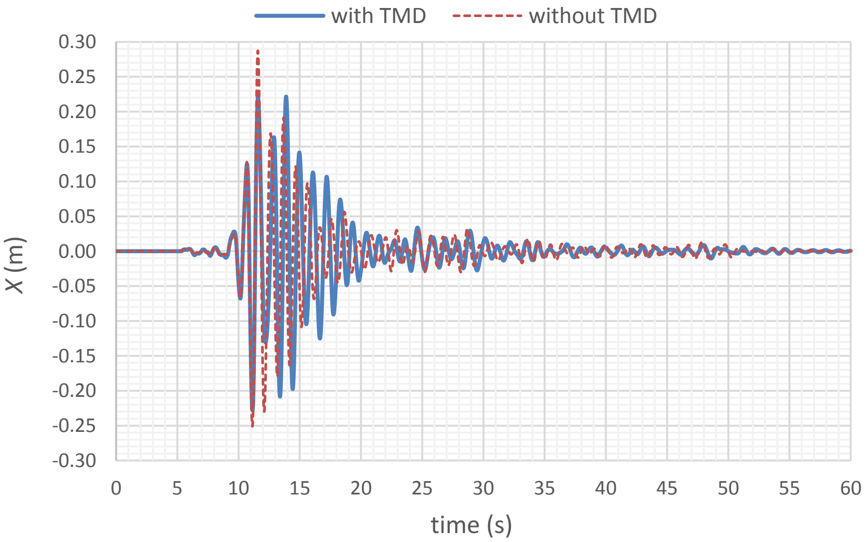

Fig. 9. Time History plots with TMD ($st_{\max}$=3.5) and without TMD cases.

4. Conclusions

According to the results, the stroke limitation is highly effective in the change of optimum TMD parameters. In order to find an economical solution, the stroke of TMD must be limited. Also, a small stroke is useful in positioning TMD. As with classical knowledge, the optimum TMD period is close to the main structure period. The optimization process generally validates this and increases the optimum TMD damping to reduce the stroke in highly limited cases. In the case of maximum damping ratio limit is not effective to reduce the stroke, the ratio of periods of TMD and structure decreases. In that case, the practical application may always be suitable to design with classical methods.

The $st_{\max}$ value (Eq. (8)) is a value that indirectly indicates the TMD's ability to move (maximum movement limit). This mobility is therefore also related to optimum TMD parameters and performance. However, the extent to which this situation will be effective depends on the external influence and the characteristics of the structural system.

As the performance of TMD in the study, a stroke limit bigger than 2.5 is not more effective than the case of $st_{\max}$=2.5. In that case, these huge stroke values are not useful, and they are very expensive to apply. The maximum displacement for critical excitation is 0.2873m and it reduces between 5.18% and 20.62% for stroke-limit cases. Also, the design that maximum reduces the displacement have a stroke value smaller than 2.75. In the cases with stroke capacity bigger than 2.75, the optimum design of TMD is the same.

Author Contributions

All of the authors made substantial contributions to conception and design, or acquisition of data, or analysis and interpretation of data; were involved in drafting the manuscript or revising it critically for important intellectual content; and gave final approval of the version to be published.

Acknowledgements

None declared.

Funding

The authors received no financial support for the research, authorship, and/or publication of this manuscript.

Conflict of Interest

The authors declared no potential conflicts of interest with respect to the research, authorship, and/or publication of this manuscript.

Data Availability

The datasets created and/or analyzed during the current study are not publicly available, but are available from the corresponding author upon reasonable request.

References

Araz O, Cakir T, Ozturk KF, Kaya D (2023). Effect of foundation embedment ratio in suppressing seismic-induced vibrations using optimum tuned mass damper. *Soil Dynamics and Earthquake Engineering*, 171, 107981.

Bekdaş G, Nigdeli SM (2017). Metaheuristic based optimization of tuned mass dampers under earthquake excitation by considering soil-structure interaction. *Soil Dynamics and Earthquake Engineering*, 92, 443–461.

Bishop RED, Welbourn DB (1952). The problem of dynamic vibration absorbers. Engineering, London 174–769.

Caicedo D, Lara-Valencia L, Blandon J, Graciano C (2021). Seismic response of high-rise buildings through metaheuristic-based optimization using tuned mass dampers and tuned mass dampers inerter. *Journal of Building Engineering*, 34, 101927.

De Domenico D, Ricciardi G (2018). Optimal design and seismic performance of tuned mass damper inerter (TMDI) for structures with nonlinear base isolation systems. *Earthquake Engineering & Structural Dynamics*, 47(12), 2539–2560.

Den Hartog JP (1949). Mechanical Vibrations. İ.T.Ü. Printing House, İstanbul.

Den Hartog JP (1956). Mechanical Vibrations. 4thed. Mc Graw-Hill, New York.

Domizio M, Garrido H, Ambrosini D (2022). Single and multiple TMD optimization to control seismic response of nonlinear structures. *Engineering Structures*, 252, 113667.

Falcon KC, Stone BJ, Simcock WD, Andrew C (1967). Optimization of vibration absorbers: a graphical method for use on idealized systems with restricted damping. *Journal of Mechanical Engineering Science*, 9(5), 374–381.

FEMA P-695 (2009). Quantification of Building Seismic Performance Factors. Federal Emergency Management Agency, Washington DC.

Frahm H (1909). Device for Damping Vibration of Bodies. US Patent 989958.

Frans R, Arfiadi Y (2015). Designing optimum locations and properties of MTMD systems. *Procedia Engineering*, 125, 892–898.

Ioi T, Ikeda K (1978). On the dynamic vibration damped absorber of the vibration system. *Bulletin of the Japanese Society of Mechanical Engineers*, 21(151), 64–71.

Khatibinia M, Akbari S, Yazdani H, Gharehbaghi S (2023). Damage-based optimal control of steel moment-resisting frames equipped with tuned mass dampers. *Journal of Vibration and Control*, 10775463221149462.

Li Y, Li S, Chen Z (2020). Optimization and performance evaluation of variable inertial tuned mass damper. *Chinese Journal of Vibration Engineering*, 33(5), 877–884.

Leung AYT, Zhang H (2009). Particle swarm optimization of tuned mass dampers. *Engineering Structures*, 31(3), 715–728.

Marian L, Giaralis A (2014). Optimal design of a novel tuned mass-damper–inerter (TMDI) passive vibration control configuration for stochastically support-excited structural systems. *Probabilistic Engineering Mechanics*, 38, 156–164.

Matlab with Simulink (2018). The MathWorks. Natick, MA.

Ormondroyd J, Den Hartog JP (1928). The Theory of Dynamic Vibration Absorber. *Transactions of ASME*, 50(7), 9–22.

Petrini F, Giaralis A, Wang Z (2020). Optimal tuned mass-damper-inerter (TMDI) design in wind-excited tall buildings for occupants' comfort serviceability performance and energy harvesting. *Engineering Structures*, 204, 109904.

Rao, R. (2016). Jaya: A simple and new optimization algorithm for solving constrained and unconstrained optimization problems. *International Journal of Industrial Engineering Computations*, 7(1), 19–34.

Soheili S, Zoka H, Abachizadeh M (2021). Tuned mass dampers for the drift reduction of structures with soil effects using ant colony optimization. *Advances in Structural Engineering*, 24(4), 771–783.

Tsai HC, Lin GC (1993. Optimum tuned - mass dampers for minimizing steady - state response of support - excited and damped systems. *Earthquake Engineering and Structural Dynamics*, 22(11), 957–973.

Villaverde R, Koyama LA (1993). Damped resonant appendages to increase inherent damping in Buildings. *Earthquake Engineering and Structural Dynamics*, 22(6), 491–507.

Warburton GB, Ayorinde EO (1980). Optimum absorber parameters for simple systems. *Earthquake Engineering and Structural Dynamics*, 8(3), 197–217.

Xu K, Igusa T (1992). Dynamic Characteristics of multiple substructure with closely spaced frequencies. *Earthquake Engineering and Structural Dynamics*, 21(12), 1059–1070.

Yücel M, Bekdaş G, Nigdeli SM (2022). Metaheuristics-based optimization of TMD parameters in time history domain. In *Optimization of Tuned Mass Dampers: Using Active and Passive Control* (pp. 55–66). Cham: Springer International Publishing.

Zucca M, Longarini N, Simoncelli M, Aly AM (2021). Tuned mass damper design for slender masonry structures: a framework for linear and nonlinear analysis. *Applied Sciences*, 11, 3425.

CHALLENGE JOURNAL OF STRUCTURAL MECHANICS 9 (4) (2023) 133–144

Research Article

Numerical investigation of the effective mechanical properties of Octet Truss lattice structures with different strut geometry

Hojjat Ghahramanzadeh Asl [a,*], Elif Altıntaş Kahriman [b,*], Derya Karaman [a]

[a] *Department of Mechanical Engineering, Karadeniz Technical University, 61080 Trabzon, Türkiye*
[b] *Department of Software Engineering, Haliç University, 34060 İstanbul, Türkiye*

ABSTRACT

Lattice structures have an important role in lightweight structure applications as they can supply their mechanical performance with less material. Porous structures designed with inspiration from nature, has been used in many industries such as aerospace, automotive, defense industry and biomedical field. In order to continue these advances, studies on various design configurations of porous structure geometries are carried out. This study aimed to increase the usage potential of Octet Truss lattice structures in various sectors. A numerical model is created for 3 variable parameters: strut geometry, porosity, and material type. The effective elastic modulus values are determined based on the principles of Hooke's law for each model. Based on the obtained effective elastic modulus values, it has been concluded that differences in strut geometries, porosities, and material types contribute to 1.27%, 68.85%, and 29.86% of the observed effects, respectively. In order to establish a correlation between these factors, the data is transmitted to the MATLAB software, where equations are generated using the curve fitting approach. A total of nine equations have been generated and the R-square for these equations above 0.99. According to the two desired constant values, the effective elastic modulus can be calculated using these equations without any restrictions.

ARTICLE INFO

Article history:
Received 4 August 2023
Revised 25 August 2023
Accepted 14 September 2023

Keywords:
Lattice structure
Effective elastic modulus
Finite element analysis
Curve fitting method
Strut geometry

1. Introduction

Porous structures are great interest today to supply the superior mechanical performance of lightweight structures (Ashby 2013). In addition to the lightness, they can supply the structure requirements by combining mechanical, thermal, and acoustic properties in one structure (Wadley 2006; Suard et al. 2015). Due to its superior properties, it has been adopted in many industrial fields such as automotive, defense, aerospace, and medical sectors (Vasiliev et al. 2012; Tao et al. 2016; Arabnejad et al. 2017). With the developments in additive manufacturing technology, porous structure applications will be encountered more frequently in more industrial areas. Porous structures have repeatable properties by combining random or regular pores into a particular solid structure (Aney et al. 2023). The randomly assembled porous structures are defined as foam structures (Langlois et al. 2018).

Regular porous structures have a wide variety of geometric configurations. For this, two basic geometric configurations are preferred by researchers: beam-based and triply periodic minimal surface (TPMS) (Majeed et al. 2022). TPMS structures are surface-based cell architectures that have surface equations and can be reproduced infinitely in Cartesian space (Al-Ketan et al 2019). Beam-based structures are cell architectures that are formed by combining various numbers of struts at different angles and nodes (Wang et al. 2020).

The positions of the struts in the structure are directly effective in the change of mechanical properties. Especially the number of struts and their positions at certain angles according to the load direction are very important in load bearing. There are lattice structures assembled in

---

* *Corresponding author.* Tel.: +90-462-377-3149 ; E-mail address: h.kahramanzade@ktu.edu.tr (H. Ghahramanzadeh Asl)

ISSN: 2149-8024 / DOI: https://doi.org/10.20528/cjsmec.2023.04.002

a unit cell at different angles and strut numbers by many researchers: such as Cube (CB), Body-Centered Cubic (BCC), Face-Centered Cubic (FCC), combination of Cube and Face-Centered Cubic (CFCC), combination of Cube and Body-Centered Cubic (CBFCC), Diamond, Octet Truss, Kelvin Rhombic dodecahedron (Zheng et al. 2019; Refai et al. 2020).

With developments in additive manufacturing, various design configurations are realized for existing lattices or new lattice structures. Wang et al., inspired by the hierarchical structures of biological materials, developed a new unit cell configuration design with an internal strut hierarchy (Wang et al. 2022). Meza et al. (2017) modeled the effect of beam geometry on Young's modulus in four beam-based lattice structures (Octet Truss, Cuboctahedron, 3D Kagome, Tetrakaidecahedron) and evaluated them in experimental and numerical analysis. With the proposed analytical model, hollow strut structures are defined as advantageous geometries in terms of mechanical properties. Wang et al. (2021) propose a new hierarchical lattice design by replacing the original straight struts of the face-centered cubic (FCC) lattice with a series of higher-level circular struts. Researchers mainly focus on modeling porous structures that will exhibit the best mechanical performance for the required design space.

In this study, the effects of strut geometry, porosity, and material type on the mechanical properties of lattice structures are investigated in Octet Truss lattice structures. Lattice structures with different porosity (60%, 70%, and 80%) are modeled using circular, hexagonal, and square geometry for the strut geometry. The effective elastic modulus of each structure is determined by the Finite Element Method according to three material properties. The obtained results are transferred to the MATLAB software and different equations are created with the curve fitting method.

2. Material and Method

2.1. Lattice structure design

According to the literature, Octet Truss Lattice models are frequently used in porous structures. The high load carrying capacity of the struts, depending on their location, is the main reason for often preferred this structures. In this study, Octet Truss lattice structures were modeled from struts in circle, hexagonal, and square geometries. Unit cells modeled at 60%, 70%, and 80% porosity were shown in Fig. 1. The unit cells were dimensioned as 1×1×1 mm^3. Porosity (P) calculation was determined by volume (Lei et al. 2020):

$$P\ (\%) = \frac{V_0 - V}{V_0} \times 100 \qquad (1)$$

In Eq. (1), V_0 is the total volume of the cubic unit cell, and V is the volume of the solid part in the lattice unit cell. Dimension values of unit cells with struts with different geometries were in Table 1.

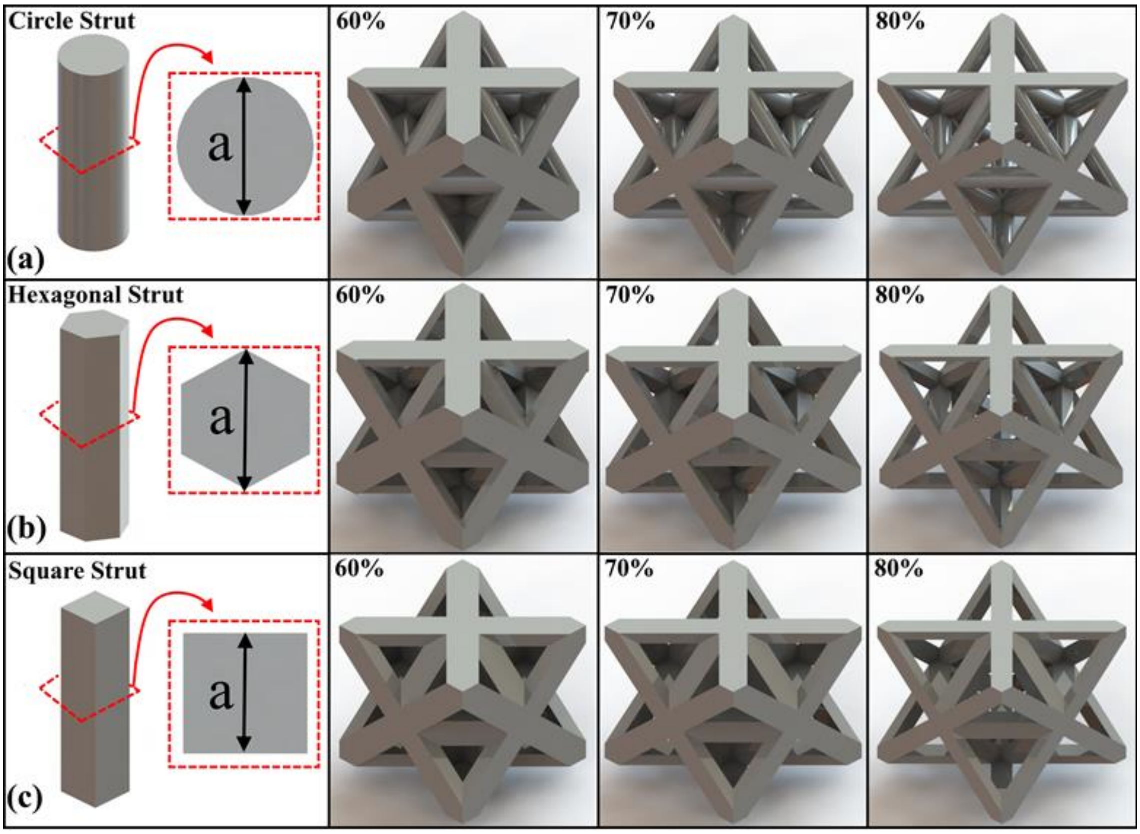

Fig. 1. Octet Truss unit cells modeled from struts of different geometry: (a) Circle; (b) Hexagonal; (c) Square.

Table 1. Dimension values of unit cells with different geometry struts (a) mm.

Strut Geometry	Porosity		
	60%	70%	80%
Circle	0.2071	0.1734	0.1368
Hexagonal	0.1973	0.1651	0.1303
Square	0.1855	0.1550	0.1220

The porosity value of the unit cells was the ratio of the available lattice structure volume to the cubic volume in a unit. Lattice structures were formed in 5x5x5 array with these unit cells in the x, y, and z directions. The terminology of these lattice structures were included in Table 2. The isometric views of the lattice structures were shown in Fig. 2.

Table 2. The terminology of lattice structure.

Porosity	Strut Geometry		
	Circle	Hexagonal	Square
60%	OctetT(c)-60	OctetT(h)-60	OctetT(s)-60
70%	OctetT(c)-70	OctetT(h)-70	OctetT(s)-70
80%	OctetT(c)-80	OctetT(h)-80	OctetT(s)-80

2.2. Finite element analysis

The material types used for the lattice structures were CP-Ti, Ti6Al4V and Stainless Steel 316L, which are commonly used in additive manufacturing technology. The mechanical properties of the materials were listed in Table 3.

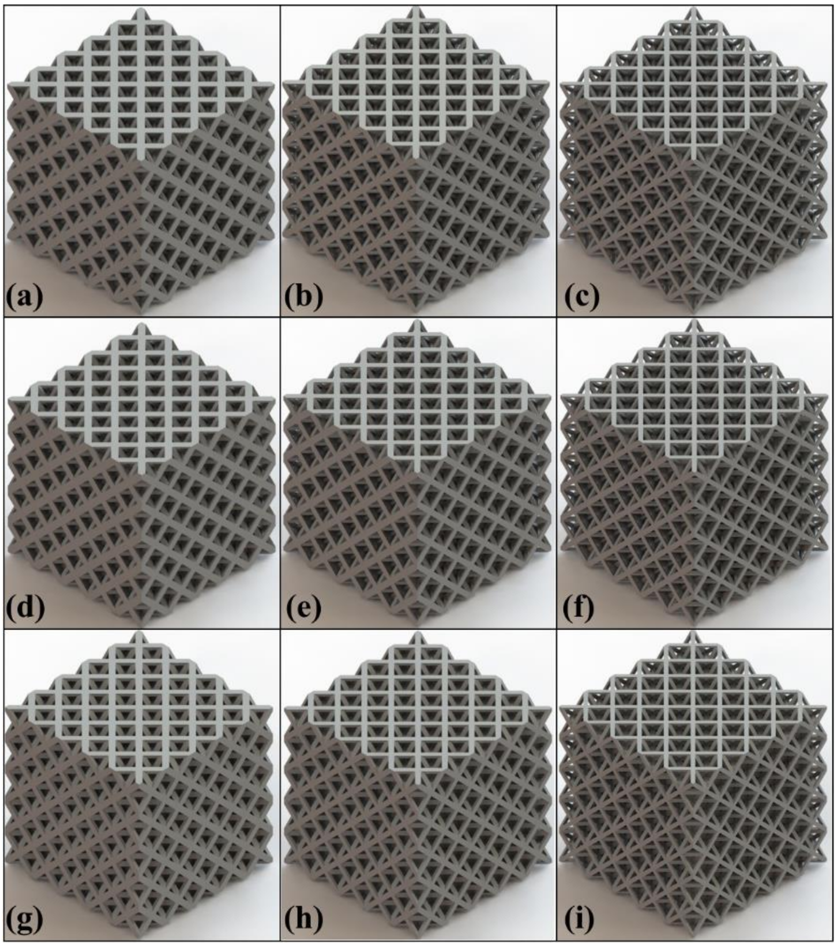

Fig. 2. Lattice structures in 5x5x5 array: (a) OctetT(c)-60; (b) OctetT(c)-70; (c) OctetT(c)-80; (d) OctetT(h)-60; (e) OctetT(h)-70; (f) OctetT(h)-80; (g) OctetT(s)-60; (h) OctetT(s)-70; (i) OctetT(s)-80.

Table 3. Mechanical properties of materials (Ma et al. 2020; Xu et al. 2019; Mercer et al. 2022).

Material	Elastic Module (GPa)	Poisson Ratio
CP-Ti	108.21	0.34
Ti6Al4V	110	0.33
Stainless Steel 316L	200	0.30
Tungsten Carbide (plate material)	600	0.21

Compression loads were applied to evaluate the mechanical properties of lattice structures. Finite element analysis method was used to determine the mechanical properties of lattice structures. Accordingly, all lattice structures were analyzed by compression load simulation using ANSYS Workbench software. As a result of these analyses, the effective elastic modulus (E_{eff}) values of each lattice structure were calculated according to Hooke's law. In Hooke's law (Eq. (2)):

$$\sigma = E \times \varepsilon$$

$$\varepsilon = \frac{\Delta L}{L_0}$$

$$E_{eff} = \left(\frac{\sigma}{\varepsilon}\right) = \frac{(\sigma \times L_0)}{\Delta L} \tag{2}$$

In Eq. (2), σ, L_0, and ΔL are the applied normal stress (MPa), the initial length of the model (mm), and directional deformation (mm), respectively.

Plates were placed at the top and bottom of each lattice structure for these simulations. The contact type between the plate and lattice structures was chosen as bonded for all simulations. The bottom plate was defined to be fixed in the x, y, and z directions. The top plate is fixed in the x and z directions and movable in the y direction. Plate geometry was designed as 5x5x1 mm. For the plates, the type of material with higher mechanical strength than the defined material was selected. A normal stress value of 1 MPa in the $-y$ direction was defined for the loading conditions (Fig. 3).

Tetrahedral elements of 0.12 mm were used for the mesh size. In the mesh convergence studies, there was no significant change in mesh sizes below 0.12 mm. Therefore, the same mesh size was used for the lattice structures. Mesh convergence analyses were carried out to achieve more stable results for beam connections and surfaces in scaffold designs where stress would be concentrated. Tetrahedral elements were used to create the mesh. The mesh quality indicated a value of 0.8784, accompanied by a standard deviation of 0.9750. Additionally, the skewness of the mesh was measured to be 0.2136, with a standard deviation of 0.1168. Fig. 4 shows the mesh structure of the lattice structures for each strut geometry.

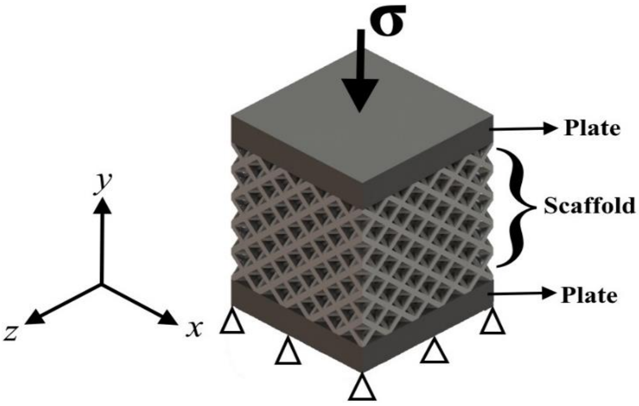

Fig. 3. Loading and boundary conditions of lattice structures.

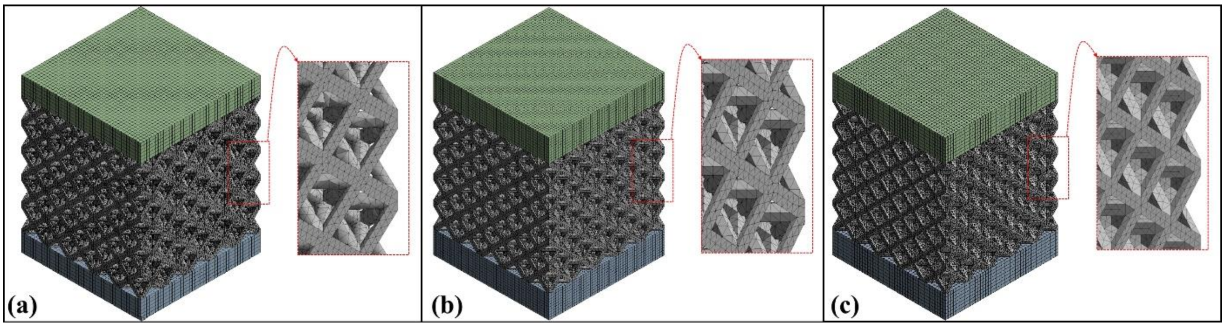

Fig. 4. Mesh structures of lattice structures with 70% porosity: (a) Circle; (b) Hexagonal; (c) Square strut geometry.

2.3. Statistical analysis

The Statistical analysis was used to determine the degree of influence of the three parameters (strut geometry, porosity, and material properties) on the effective elastic modulus of Octet Truss lattice structures. The statistical methodology used to investigate the observed differences was the one-way analysis of variance (ANOVA). $p<0.05$ was considered as a statistically significant difference. In this analysis, the signal value (S) is the value to be measured, and the noise value (N) is the effectiveness of the undesired factors within the measured value. The graphs of the calculated S/N ratios represent the degree of influence of any variable parameter used in the analysis. In addition to the S/N ratio, ANOVA analysis was used to determine the significance levels of variable parameters affecting the mechanical properties of the structures. This analysis was performed with Minitab software.

2.4. Curve fitting application

Curve fitting is a machine learning approach that is often used in the field of data science. It was used to find the optimum fit by investigating the correlation between the dependent and independent variables. The points in the dataset were also utilized to create a curve-shaped linear or nonlinear mathematical function. The statistical correlations used for the data analysis are the sum of squared errors (SSE), R-squared (R^2), adjusted Rsquare, and root mean square error ($RMSE$). The RMSE approach was used in the following equation (Eq. (3)) to define the error:

$$RMSE = \sqrt{\frac{\sum_{i=1}^{N}(\hat{y}_i - y_i)^2}{N}} \tag{3}$$

where N is the total number of training data, y_i is the data value at time t_i, $\hat{y}_i$ is the predicted value at time t_i.

The following equation was used to determine the error value.

$$\text{Error Value} = \frac{(\text{Actual Value} - \text{Value Obtained by Curve Fitting})}{\text{Actual Value}} \; x\, 100 \qquad (4)$$

In this study, (X, Y, and Z) were used as input factors. The data from each lattice structure model for all materials and porosities were analyzed using MATLAB software. For each type of lattice structure, the initial curve fittings were developed. These curve fittings utilized of the material's elastic modulus for the X value (108210, 110000, and 200000), the porosity for the Y value (60, 70, and 80), and the measured effective elastic modulus for the Z value. The second curve fittings were obtained while taking the materials into account; in this case, the lattice structure types (Octet Truss-Circle (1), Octet Truss-Hexagonal (2), and Octet Truss-Square (3)) were taken into account as "x," "y" values are porosity rates (60, 70, and 80), and "z" values are effective elastic modulus values. The third curve fittings took porosity into account. Therefore, "x" parameter represented different types of lattice structures (1, 2, and 3), "y" values represented different elastic modulus (108210, 110000, and 200000), and "z" values represented measurements of the effective elastic modulus values. Additionally, these models' functions were constructed in the MATLAB programming language as 2nd order polynomials.

3. Results and Discussions

Compression loads for three types of materials were simulated for Octet Truss lattice structures in different strut geometries and different porosity. The maximum von-Mises stress values obtained by finite element analysis were listed in Table 4. Stress values increased with increasing porosity for each geometry type.

For same material type in Octet Truss lattice structure, strut geometry was an effect on stress generation. At the same porosity ratios, the lowest stress occurred in square geometries, and the highest stress value occurred in hexagonal geometry lattice structure. Considering the effect of strut geometry for Cp-Ti material: There was 27.54% difference between OctetT(s)-60 and OctetT(c)-60, and 18.78% difference between OctetT(c)-60 and OctetT(h)-60 for 60% porosity. There was 23.55% difference between OctetT(s)-70 and OctetT(c)-70, and 20.31% difference between OctetT(c)-70 and OctetT(h)-70 for 70% porosity. There was 4.75% difference between OctetT(s)-80 and OctetT(c)-80, and 20.08% difference between OctetT(c)-80 and OctetT(h)-80 for 80% porosity. This difference situation was similar for other material types. The maximum stress values in lattice structures with the same porosity changed according to the material type. There was not significant difference between CP-Ti and Ti6Al4V materials. This was related to the mechanical properties of these materials close to each other. Lattice structures with 316L steel material had relatively lower stresses compared to other materials. This was due to the high elastic modulus of this material. The distribution contours of these stress values on the lattice structures were shown in Fig. 5.

In Octet Truss lattice structures with the same porosity, the directional deformation value was affected by the strut geometry. Directional deformation occurring in lattice structures with the same porosity was lowest in square geometries and highest in circle geometries. Considering the effect of strut geometry for Ti6Al4V material: There was 12.26% difference between OctetT(s)-60 and OctetT(h)-60, and 4.29% difference between OctetT(h)-60 and OctetT(c)-60 for 60% porosity. There was 8.69% difference between OctetT(s)-70 and OctetT(h)-70, and 5.75% difference between OctetT(h)-70 and OctetT(c)-70 for 70% porosity. There was 8.61% difference between OctetT(s)-80 and OctetT(h)-80, and 5.96% difference between OctetT(h)-80 and OctetT(c)-80 for 80% porosity. These difference ratios could be considered the same for other materials. Considering the material effect on directional deformation, a difference of approximately ~2% was detected for the same porosity ratios for CP-Ti and Ti6Al4V materials. However, when these two material types are compared with the 316L material, the difference value has increased. So, the approximate difference between 316L lattice structures and lattice structures with the same porosity as CP-Ti or Ti6Al4V material was ~85%. The distribution contours of the directional deformations in the lattice structures were shown in Fig. 6.

At the same time, directional deformation (-y) values of each lattice structure were recorded by the finite element analysis (Table 5). The occurrence of directional deformation increased with increase porosity.

Table 4. von-Mises stresses in lattice structures according to material type (MPa).

Lattice structure	CP-Ti	Ti6Al4V	316L
OctetT(c)-60	16.795	16.759	16.678
OctetT(c)-70	25.998	25.959	25.911
OctetT(c)-80	43.327	43.314	44.212
OctetT(h)-60	19.949	19.994	20.085
OctetT(h)-70	31.278	31.277	31.269
OctetT(h)-80	52.027	52.383	53.679
OctetT(s)-60	13.168	13.155	13.109
OctetT(s)-70	21.042	21.025	21.025
OctetT(s)-80	41.364	41.692	42.957

Table 5. Directional deformation in lattice structures according to material type (mm).

Lattice structure	CP-Ti	Ti6Al4V	316L
OctetT(c)-60	393.75 E-6	387.76 E-6	208.54 E-6
OctetT(c)-70	647.98 E-6	638.10 E-6	344.81 E-6
OctetT(c)-80	1182.80 E-6	1164.70 E-6	631.77 E-6
OctetT(h)-60	377.42 E-6	371.80 E-6	201.05 E-6
OctetT(h)-70	612.59 E-6	603.42 E-6	327.41 E-6
OctetT(h)-80	1116.10 E-6	1099.20 E-6	596.96 E-6
OctetT(s)-60	336.42 E-6	331.20 E-6	178.31 E-6
OctetT(s)-70	563.94 E-6	555.19 E-6	300.24 E-6
OctetT(s)-80	393.75 E-6	387.76 E-6	208.54 E-6

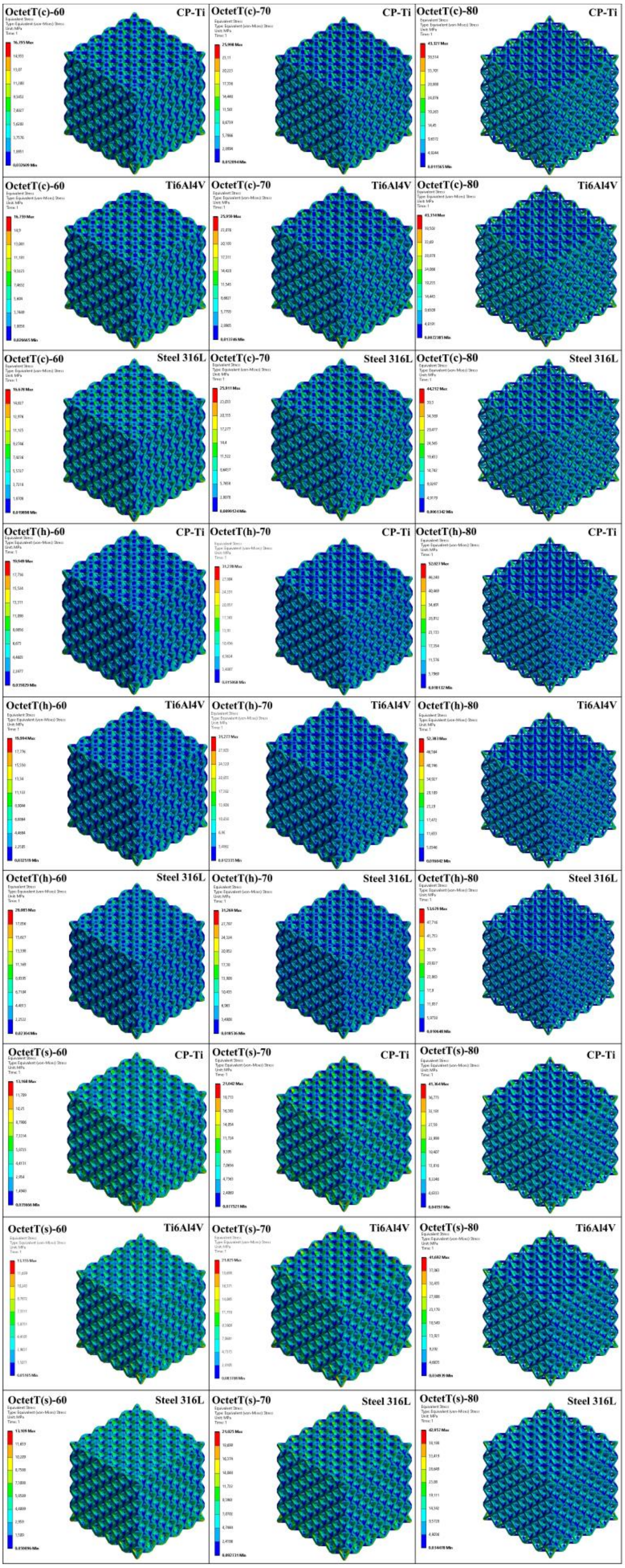

Fig. 5. Distribution contours of these von-Mises stress values on the lattice structures.

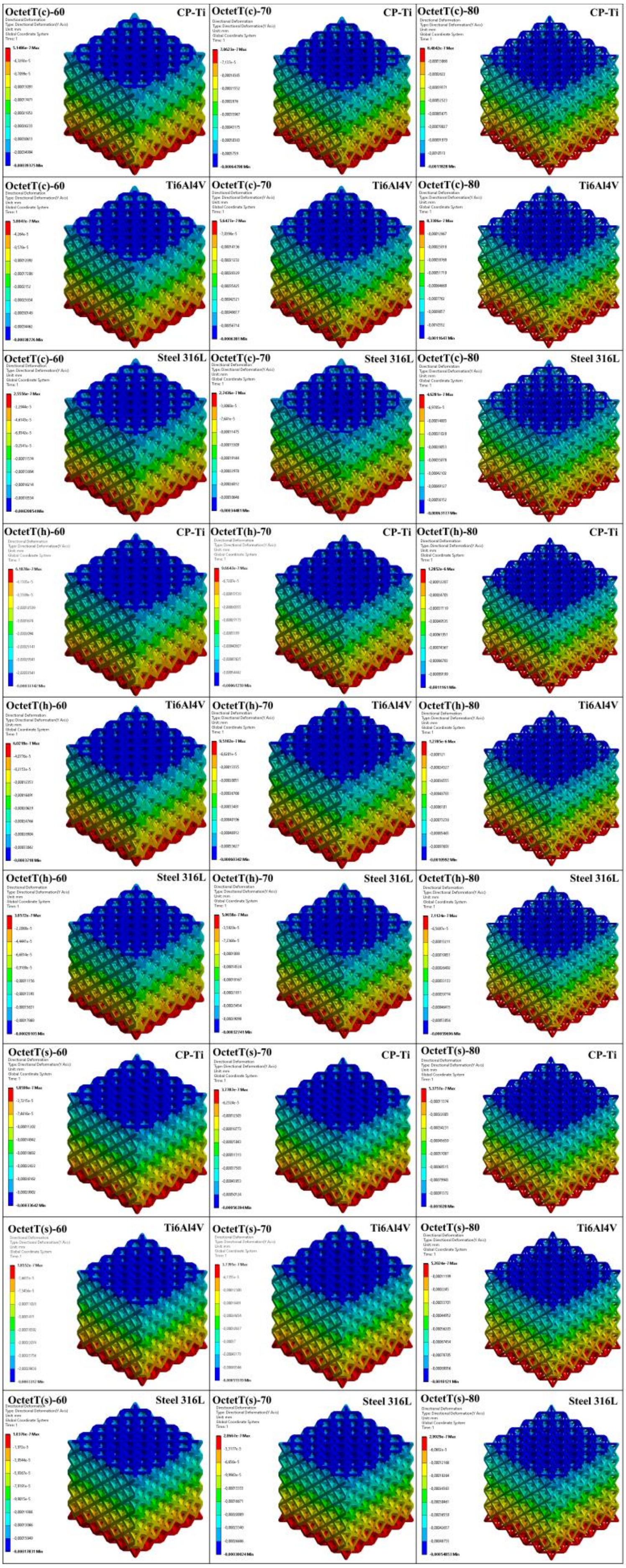

Fig. 6. Distribution contours of these directional deformation values on the lattice structures.

The effective elastic modulus of the lattice structure was calculated according to Hooke's law. Calculations were performed according to the directional deformation values listed in Table 5. The graphs of the effective elastic modulus of the lattice structures grouped by material type were shown in Fig. 7. Lattice structures with CP-Ti and Ti6Al4V materials had effective elastic modulus close to each other. Among lattice structures of the same strut geometry and porosity, Ti614V lattice structures had as much as 1.5% greater elasticity than CP-Ti. 316L stainless Steel lattice structures had the highest effective elastic modulus in this material group. Compared to Cp-Ti and Ti6Al4V lattice structures, it had approximately 85% more elastic modulus. This was due to the lattice structures were inversely proportional to the directional deformation. According to the deformations listed in Table 5, the lowest values belonged to the lattice structures with 316L material. This was a clear indication that the mechanical properties of the materials were an influential parameter for mechanical performance in porous structures.

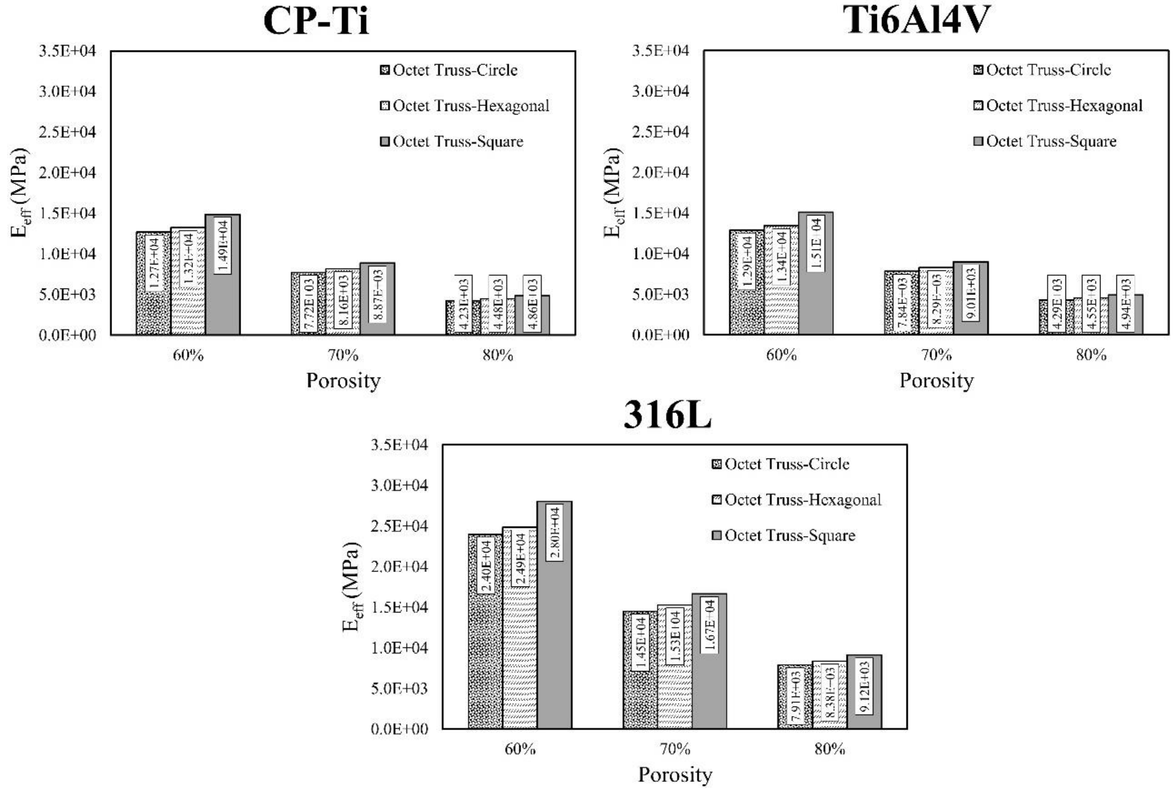

Fig. 7. Effective elastic modulus of Octet Truss lattice structures with different strut geometry, determined by material type.

As the porosity of the lattice structures increased, a decrease was observed in the mechanical behavior due to the reduced cross-sectional area of the structures (Maskery et al. 2018). This was known with the results of experimental and numerical analyzes applied in studies (Günther et al. 2022; Park et al. 2022; Bai et al. 2020). Load-bearing areas decreased as porosity increased and structural volume decreased (Zao et al. 2018). This was clearly seen in Octet Truss lattice structures in different geometries. The effective elastic modulus decreased for each type of strut geometry with increasing porosity from 60% to 80%. This decrease occurred at approximately the same rates for each strut geometry. A reduction of approximately ~39% compared to 60% lattice structures at 70%, and approximately ~45% reduction at 80% compared to 70% lattice structures was determined.

It was noted that the strut geometry is an effective parameter for the effective elastic modulus. So, the values with the same porosity for a material type were confirmation of this. The effective elastic modulus value of the lattice structures with the same porosity ratios was the lowest in the circle geometry and the highest in the square geometry. The different values caused by the strut geometries had approximately the same rate of variation for the three material types. Considering the effect of strut geometry for 316L material: There was an increase 3.73% between OctetT(c)-60 and OctetT(h)-60, and an increase 12.75% between OctetT(h)-60 and OctetT(s)-60 for 60% porosity. There was an increase 5.31% between OctetT(c)-70 and OctetT(h)-70, and an increase 9.05% between OctetT(h)-70 and OctetT(s)-70 for 70% porosity. There was an increase 5.83% between OctetT(c)-80 and OctetT(h)-80, and an increase 8.83% between OctetT(h)-80 and OctetT(s)-80 for 80% porosity.

As it could be understood from the results obtained by numerical analysis, the strut geometry, porosity, and material type parameters affected the mechanical performance of the lattice structures at different rates. Statistical analysis results were given in Fig. 8 to understand the degree of influence of the three parameters. A residual error of 0.02% was found in generating the S/N ratio charts. For Octet Truss lattice structures, strut geometry, porosity and material type parameters had 1.27%, 68.85% and 29.86% effects on the mechanical performances of the lattice structures, respectively. In this statement, the signal value (S) is the value to be measured, and the noise value (N) is the effectiveness of the undesired factors within the measured value. The graphs of the calculated S/N ratios represent the degree of influence of any variable parameter used in the analysis. In addition to the S/N ratio, ANOVA analysis was used to determine the significance levels of variable parameters affecting the mechanical properties of the structures. This analysis was performed with Minitab software.

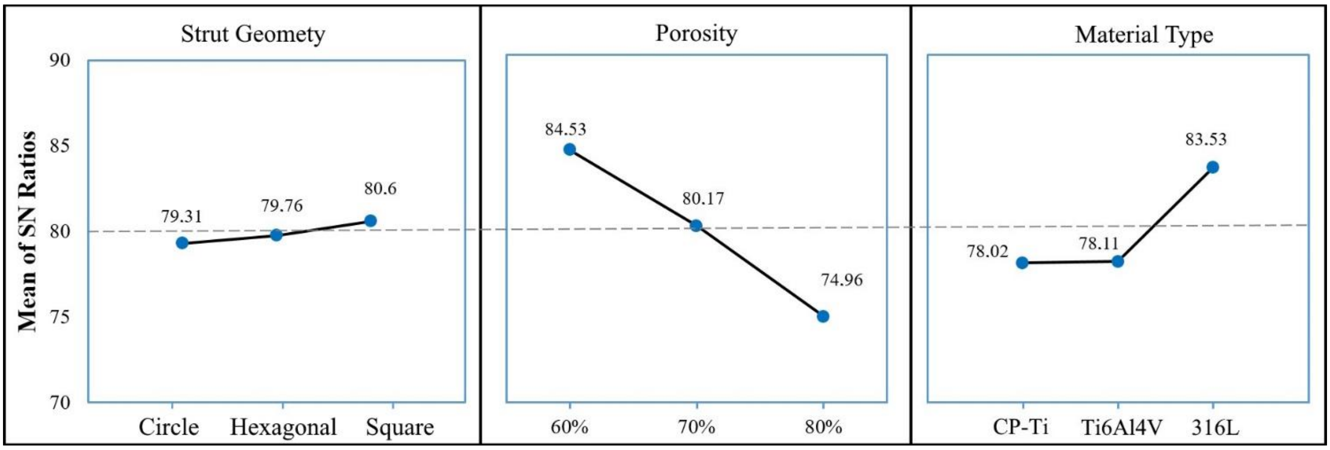

Fig. 8. Effect of strut geometry, porosity and material type parameters on effective elastic modulus for Octet Truss lattice structures.

The effective elastic modulus values were inputted into the MATLAB program in order to create a correlation between results. The equations for each lattice structure were generated using the curve fitting technique in the MATLAB program, considering consideration of all materials and porosities. The following equations and R squared values for each lattice structures were shown in Table 6 when the "x" value is taken as the elastic modulus of materials (MPa) and the "y" value is taken as porosity rates (%). These curve fitting findings were represented graphically in Fig. 9. Table 6 provides equations that are used to calculate the effective elastic modulus of lattice structures depending on the material's elastic modulus value and the desired amount of porosity.

Table 6. Curve fitting analysis results in terms of lattice structure type.

Lattice structure type	Curve fitting equation	R-square
Octet Truss-Circle	$f_1(x,y,z) = (4.736\,E+4) + 0.3415\,x + (-1351)\ y + (8.857\,E-8)\,x^2 + (-0.00414)\ x\,y + 9.83\,y^2$	0.9993
Octet Truss-Hexagonal	$f_2(x,y,z) = (4.518\,E+4) + 0.3465\,x + (-1272)\ y + (9.949\,E-8)\,x^2 + (-0.004214)\ x\,y + 9.218\,y^2$	0.9994
Octet Truss-Square	$f_3(x,y,z) = (6.296\,E+4) + 0.4059\,x + (-1809)\ y + (8.561\,E-8)\,x^2 + (-0.004867)\ x\,y + 13.11\,y^2$	0.9991

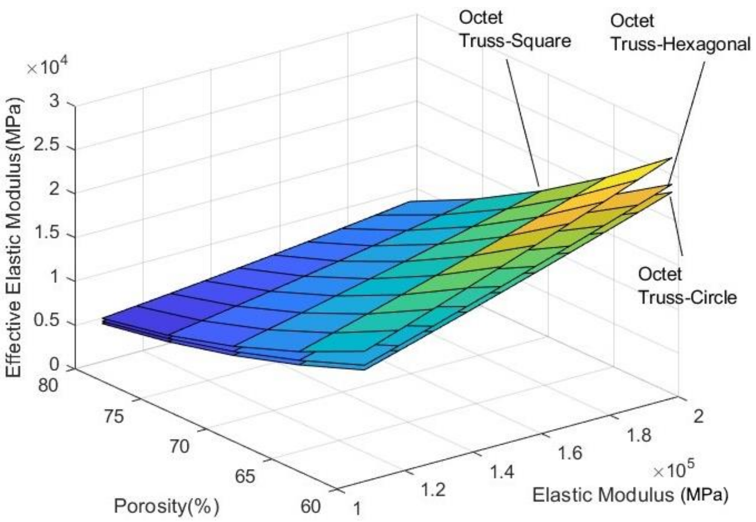

Fig. 9. The graphics of curve fitting results for each lattice structure models.

Equations were developed for the second analysis based on the elastic modulus of each material. For each material, "x" and "y" variables representing lattice structure types and porosities were accepted in these studies. Table 7 provides the curve-fitting formulae and R-squared values in accordance with the results. Additionally, graphs invented of MATLAB curve fitting formulae for each material attribute were provided in Fig. 10. With the lattice structure type and the desired amount of porosity entered into the formulae found in Table 7, it will be feasible to determine how much effective elastic modulus lattice structures will possess.

Table 7. Curve fitting analysis results in terms of material properties.

Elastic modulus of materials	Curve fitting equation	R-square
316L	$g_1(x,y,z) = (1.419\,E+5) + 4136\,x + (-2918)\;y + 528\,x^2 + (-71.6)\;x\,y + 15.74\,y^2$	0.9989
CP-Ti	$g_2(x,y,z) = (7.411\,E+4) + 2362\,x + (-1519)\;y + 242.5\,x^2 + (-38.19)\;x\,y + 8.151\,y^2$	0.9991
Ti6A14V	$g_3(x,y,z) = (7.525\,E+4) + 2391\,x + (-1542)\;y + 250\,x^2 + (-38.87)\;x\,y + 8.276\,y^2$	0.9991

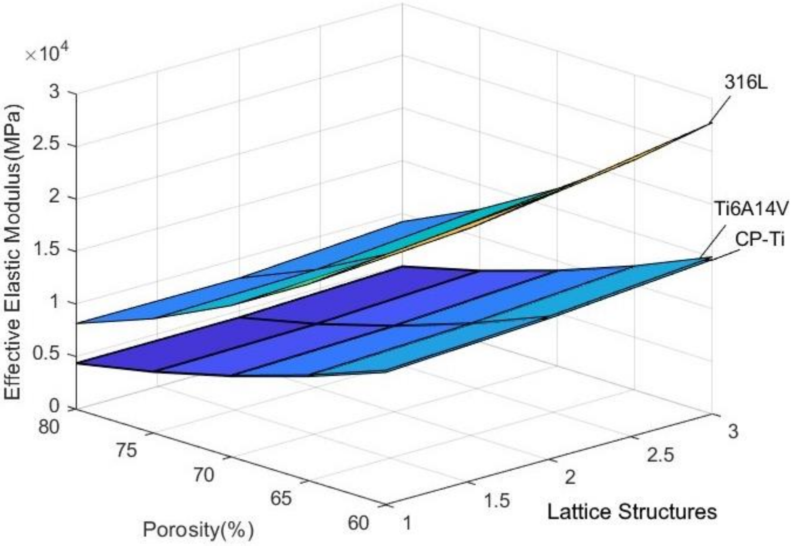

Fig. 10. The graphics of curve fitting results for each material properties.

In the end, the "x" and "y" parameters represent the various types of lattice structures and the elastic modulus of materials, respectively. As a result, each porosity's results were investigated independently. The curve fitting equations and R-squared values for each porosity were provided in Table 8 below. Additionally, the graphs obtained by these curve-fitting equations were shown in Fig. 11. By choose the lattice structure type and the elastic modulus of the material to be design according to the equations in Table 7, the effective elastic modulus values of the lattice structure will be determined.

Table 8. Curve fitting analysis results in terms of porosities.

Porosity	Curve fitting equation	R-square
60%	$h_1(x,y,z) = 5232 + (-2997)\,x + 0.06382\,y + 739.8\,x^2 + 0.01035\,x\,y + (1.508\,E-08)\,y^2$	0.9994
70%	$h_2(x,y,z) = 2164 + (-775.1)\,x + 0.04259\,y + 189.9\,x^2 + 0.00546\,x\,y + (18.184\,E-08)\,y^2$	0.9998
80%	$h_2(x,y,z) = 1092 + (-377.9)\,x + 0.0242\,y + 90.83\,x^2 + 0.003075\,x\,y + (4.097\,E-08)\,y^2$	0.9999

Tables 6, 7, and 8 show that the equations have R-square values of more than 0.99. The term with a low degree of effect compared to the others could be removed from these equations. So that results could be obtained with simpler equations. Since this affects the R^2 values of the equations, the equations presented in the study were given with all the details. These figures show that the data used to create the graphs was sufficiently similar to each other. This finding was supported by a closer look at the current study's reaction surface plots (Karaman et al. 2022). These investigations also provide researchers with a reliable mathematical model to estimate these parameters of the input and output for any response value before executing actual tests.

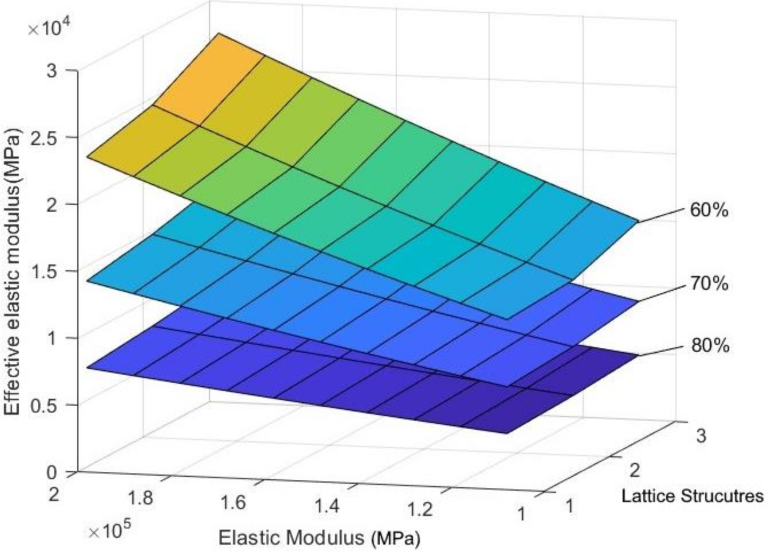

Fig. 11. The graphics of curve fitting results for each porosity.

4. Conclusions

In this study, the effects of strut geometry, porosity, and material type on the mechanical performance of lattice structures were numerically investigated. The porosities of circular, hexagonal, and square Octet Truss lattice structures were modeled at 60%, 70%, and 80%, respectively. A total of 27 numerical analyzes were performed with three different material types. As a result of the analyses, the effective elastic modulus of the lattice structures were determined according to Hooke's law. It was determined by ANOVA analysis that the strut geometry, porosity and material type parameters had 1.27%, 68.85% and 29.86% effects on the mechanical performances of the lattice structures, respectively. In accordance with the curve fitting technique used for the data produced by finite element analysis, three kinds of polynomial 2nd-order curve equations were developed. A total of nine equations were found, and their R-square values exceeded 0.99. Using two desirable constant values and the nine equations that were found, the effective elastic modulus could be determined. For the engineering industries, especially in the biomedical engineering application, the accuracy of the correlations found for each curve equation was satisfactory. Since there are several options for the geometric and mechanical characteristics of the structure, these curve equations are a reliable tool in design and manufacture planning for a quick manufacturing process.

Author Contributions

All of the authors made substantial contributions to conception and design, or acquisition of data, or analysis and interpretation of data; were involved in drafting the manuscript or revising it critically for important intellectual content; and gave final approval of the version to be published.

Acknowledgements

None declared.

Funding

The authors received no financial support for the research, authorship, and/or publication of this manuscript.

Conflict of Interest

The authors declared no potential conflicts of interest with respect to the research, authorship, and/or publication of this manuscript.

Data Availability

The datasets created and/or analyzed during the current study are not publicly available, but are available from the corresponding author upon reasonable request.

References

Al-Ketan O, Abu Al-Rub RK (2019). Multifunctional mechanical metamaterials based on triply periodic minimal surface lattices. *Advanced Engineering Materials*, 21(10), 1900524.

Aney S, & Rege A (2023). The effect of pore sizes on the elastic behaviour of open-porous cellular materials. *Mathematics and Mechanics of Solids*, 28(7), 1624-1634.

Arabnejad S, Johnston B, Tanzer M, Pasini D (2017). Fully porous 3D printed titanium femoral stem to reduce stress-shielding following total hip arthroplasty. *Journal of Orthopaedic Research*, 35(8), 1774-1783.

Ashby M (2013). Designing architectured materials. *Scripta Materialia*, 68(1), 4-7.

Bai L, Gong C, Chen X, Sun Y, Xin L, Pu H, Luo J (2020). Mechanical properties and energy absorption capabilities of functionally graded lattice structures: Experiments and simulations. *International Journal of Mechanical Sciences*, 182, 105735.

Günther F, Wagner M, Pilz S, Gebert A, Zimmermann M (2022). Design procedure for triply periodic minimal surface based biomimetic scaffolds. *Journal of the Mechanical Behavior of Biomedical Materials*, 126, 104871.

Karaman D, Ghahramanzadeh Asl H, Altıntaş Kahriman E (2022). Estimation and Comparison of Effective Elastic Modulus of Different Scaffolds Using Curve Fitting Method for Additive Manufacturing Field. *Arabian Journal for Science and Engineering*, 47, 15973-15987.

Langlois V, Trinh VH, Lusso C, Perrot C, Chateau X, Khidas Y, Pitois O (2018). Permeability of solid foam: Effect of pore connections. *Physical Review E*, 97(5), 053111.

Lei HY, Li JR, Xu ZJ, Wang QH (2020). Parametric design of Voronoi-based lattice porous structures. *Materials & Design*, 191, 108607.

Ma TH, Chang L, Guo S, Kong LR, He XH, Zhou CY (2020). Comparison of multiaxial low cycle fatigue behavior of CP-Ti under strain-controlled mode at different multiaxial strain ratios. *International Journal of Fatigue*, 140, 105818.

Majeed M, Khan HM, Wheatley G, Situ R (2022). Influence of post-processing on additively manufactured lattice structures. *Journal of the Brazilian Society of Mechanical Sciences and Engineering*, 44(9), 389.

Maskery I, Sturm L, Aremu AO, Panesar A, Williams CB, Tuck CJ, Hague RJ (2018). Insights into the mechanical properties of several triply periodic minimal surface lattice structures made by polymer additive manufacturing. *Polymer*, 152, 62-71.

Mercer C, Speck T, Lee J, Balint DS, Thielen M (2022). Effects of geometry and boundary constraint on the stiffness and negative Poisson's ratio behaviour of auxetic metamaterials under quasi-static and impact loading. *International Journal of Impact Engineering*, 169, 104315.

Meza LR, Phlipot GP, Portela CM, Maggi A, Montemayor LC, Comella A, Greer JR (2017). Reexamining the mechanical property space of three-dimensional lattice architectures. *Acta Materialia*, 140, 424-432.

Park SJ, Lee JH, Yang J, Heogh W, Kang D, Yeon SM, Park J (2022). Lightweight injection mold using additively manufactured Ti-6Al-4V lattice structures. *Journal of Manufacturing Processes*, 79, 759-766.

Refai K, Montemurro M, Brugger C, Saintier N (2020). Determination of the effective elastic properties of titanium lattice structures. *Mechanics of Advanced Materials and Structures*, 27(23), 1966-1982.

Suard M, Martin G, Lhuissier P, Dendievel R, Vignat F, Blandin JJ, Villeneuve F (2015). Mechanical equivalent diameter of single struts for the stiffness prediction of lattice structures produced by Electron Beam Melting. *Additive Manufacturing*, 8, 124-131.

Tao W, Leu MC (2016). Design of lattice structure for additive manufacturing. *In 2016 International Symposium on Flexible Automation,* USA, 325-332.

Vasiliev VV, Barynin VA, Razin AF (2012). Anisogrid composite lattice structures–Development and aerospace applications. *Composite structures*, 94(3), 1117-1127.

Wadley HN (2006). Multifunctional periodic cellular metals. Philosophical Transactions of the Royal Society A: Mathematical. *Physical and Engineering Sciences*, 364(1838), 31-68.

Wang P, Bian Y, Yang F, Fan H, Zheng B (2020). Mechanical properties and energy absorption of FCC lattice structures with different orientation angles. *Acta Mechanica*, 231, 3129-3144.

Wang P, Yang F, Ru D, Zheng B, Fan H (2021). Additive-manufactured hierarchical multi-circular lattice structures for energy absorption application. *Materials & Design*, 210, 110116.

Wang M, Zhang J, Wang W, Gao L (2022). Compression behaviors of the bio-inspired hierarchical lattice structure with improved mechanical properties and energy absorption capacity. *Journal of Materials Research and Technology*, 17, 2755-2771.

Xu Y, Zhang D, Hu S, Chen R, Gu Y, Kong X, Jiang Y (2019). Mechanical properties tailoring of topology optimized and selective laser melting fabricated Ti6Al4V lattice structure. *Journal of the mechanical behavior of biomedical materials*, 99, 225-239.

Zhao M, Liu F, Fu G, Zhang DZ, Zhang T, Zhou H (2018). Improved mechanical properties and energy absorption of BCC lattice structures with triply periodic minimal surfaces fabricated by SLM. *Materials*, 11(12), 2411.

Zheng HD, Liu LL, Deng CL, Shi ZF, Ning CY (2019). Mechanical properties of AM Ti6Al4V porous scaffolds with various cell structures. *Rare Metals*, 38, 561-570.

Challenge Journal of Structural Mechanics 9 (4) (2023) 145–152

Challenge Journal of Structural Mechanics

Research Article

Fuzzy logic based prediction of retaining wall stability

Esra Aslı Çubukçu [a,*], Esra Uray [a], Vahdettin Demir [a]

[a] *Department of Civil Engineering, KTO Karatay University, 42020 Konya, Türkiye*

ABSTRACT

In geotechnical engineering, retaining walls are widely employed to solve the problem of supporting horizontal loads occurring between two different soil levels. In the traditional retaining wall design, stability checks continue until a safe design is obtained according to selected wall dimensions and soil properties. This design method is a process that is time-consuming and based on trial and error. In this study, the stability control of the retaining wall, which is a complex engineering design, has been carried out with fuzzy logic methods. Adaptive network-based fuzzy inference systems (ANFISs) including Grid Partition (ANFIS-GP) and Substructive Clustering (ANFIS-SC) have been utilized as fuzzy logic methods. The sliding stability criterion of the cantilever retaining wall has been obtained by performing 1024 retaining wall designs which are created using different wall dimensions. Ninety percent and ten percent of the 1024 sliding safety factor values acquired through numerical analyses were respectively allocated to the training and testing phases. The prediction performances of the methods have been evaluated by considering the Root Mean Square Error (*RMSE*), Mean Absolute Error (*MAE*), and Coefficient of Determination (R^2) obtained for the sliding safety factors during the training and testing stages. Upon juxtaposing the actual and anticipated sliding safety factors for a dataset comprising 1024 observations, it has become evident that the ANFIS-SC methodology outperforms the ANFIS-GP approach in terms of predictive accuracy. Furthermore, this analysis culminated in the determination that the application of fuzzy logic methods stands as an efficacious and dependable means for checking the stability criteria of retaining walls.

ARTICLE INFO

Article history:
Received 30 May 2023
Revised 21 July 2023
Accepted 14 October 2023

Keywords:
Retaining wall design
Stability check
Fuzzy logic
Artificial intelligence

1. Introduction

Retaining walls, which are an engineering structure, are mainly employed in developing and expanding cities, on highway and railway transportation lines, in engineering structures such as bridges and roads, in coastal areas, and in irrigation canals. It is constructed as a vertical structural element in places where it is not possible to connect two different floors with a slope (Fig. 1). These structures are of vital importance in order to prevent negative situations that may affect the current structure during the operation process by ensuring the safety of work and worker health and stability, temporary or permanent as soon as the works and productions continue. In this mission, which is assigned to geotechnical engineers, a proactive approach is required to anticipate possible collapse scenarios and to analyze and implement designs that are safe against these scenarios. Lateral soil pressure theories put forward by the researchers are used to understand the natural behavior of the soil and to analyze the collapse scenarios correctly (Das and Sivakugan 2017).

Several parameters are decisive in the formation of lateral soil pressures affecting the retaining structures. These are the behavior of the soil under load, the engineering parameters such as the shear resistance of the soil, the physical properties of the soil, the groundwater condition, the geometry of the retaining structure drainage conditions, and external effects. In the case of transport or movement in the soil environment, stress

---

* *Corresponding author*. E-mail address: cubukasli@gmail.com (E. A. Çubukçu)

ISSN: 2149-8024 / DOI: https://doi.org/10.20528/cjsmec.2023.04.003

changes and discharges occurring in the force balance of the system in the transport or movement region cause stability problems (Sağlamer 1985).

In geotechnical engineering, retaining structures are used to prevent the negative effects of the abovementioned stability problem. In the conventional stability control of the retaining wall, the repeated trial-and-error method is utilized according to the selected wall pre-sizing until the safe design is achieved. In traditional calculation methods, it is a problem that the designs made by trial and error based on experience take a long time and economic sections cannot be obtained. By making use of information technologies, the design processes can become faster and more reliable, and at the same time, it is possible to reduce the negative situations affecting nature by using the resources correctly by conducting interdisciplinary studies with the developing technology. In general, like all engineering structures, the traditional calculation methods of retaining walls take a long time and increase the workload of geotechnical engineers.

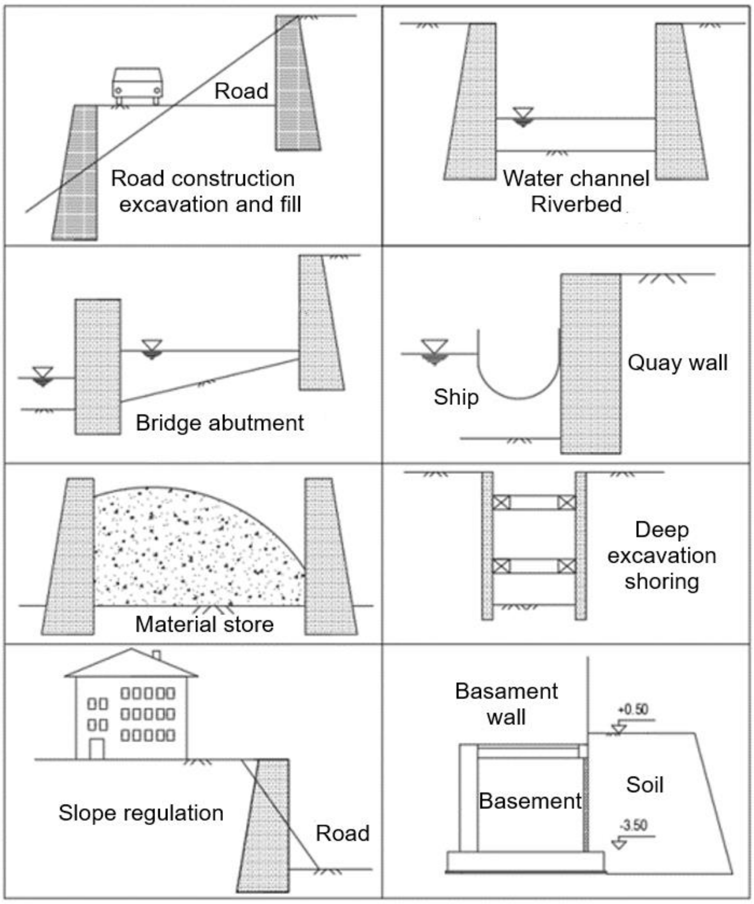

Fig. 1. Retaining structure applications (Uray 2020).

This phenomenon has drawn the attention of many researchers, and with the help of algorithms used for this problem, the processing power of computers has been emphasized and it has been stated that it is possible to obtain safe and fast results with multidisciplinary studies (Binici and Öztürk 2019; Uray et. al 2021, 2022). In addition, there are many studies in the literature on the variation of analysis results under different soil conditions and other variables in retaining wall design (Arama et al. 2020; Arslan et al. 2018; Dağdeviren and Kaymak 2018; Gandomi et al. 2015; Uray et al. 2019a; Yepes et al. 2008). Studies with methodologies such as the use of artificial neural networks, the use of heuristic optimization methods, the use of various optimization algorithms, and the realization of predictions with machine learning are included in the literature (Shahin et al. 2009; Manjunath et al. 2012; Önalp and Arel 2012; Gokkus et al. 2018; Uray et al. 2019b; Seyhan 2021; Mishra et al. 2021; Mustafa et al. 2022). Çıtakoğlu and Coşkun (2021) made predictions for the future by using the monthly total precipitation data between the years 1990–2015. They made the prediction model using traditional ANN and ANFIS, followed by wavelet transform ANN and wavelet transform ANFIS. The prediction performances of these models were evaluated according to statistical criteria. Predictions made using ANN and ANFIS methods did not yield the desired result. According to the coefficient of determination, Wavelet transform ANN (DD–ANFIS) and wavelet transform ANFIS (DD–ANFIS) models were found to be more successful in predicting future precipitation data (Citakoglu and Coskun 2021). Citakoglu et al. (2014) created a monthly average evaporation model using ANN and ANFIS models. Various combinations of long-term average monthly climate data such as wind speed, air temperature, relative humidity and solar radiation were used as input parameters in the models. It was observed that the ANFIS and ANN model gave more successful results compared to the results compared with the classical method (Citakoglu et al. 2014). Başakın et al. (2022) analyzed the monthly wind speed time series of Kırşehir province using independent, hybrid and ensemble models. Artificial neural networks, Gaussian process regression, support vector machines and multivariate adaptive regression lines are used as stand-alone machine learning models, while discrete wavelet transform is used as a preprocessing technique to create hybrid models. The results revealed that hybrid wavelet models outperform independent models (Başakın et al. 2022).

In the engineering discipline, effective, economical, and aesthetic design is essential, as well as minimizing the negative situations affecting nature by acting with the principle of sustainability. Providing a state of safety with economic sections is beneficial in this regard. In this study, the prediction of the sliding safety factor of the cantilever retaining wall against sliding was investigated employing two different fuzzy logic methods. The performance of the methods was examined by statistically evaluating the predicted sliding safety factor.

2. Method

2.1. Cantilever retaining wall

In the traditional solution method of the retaining structures, the preliminary design given in Fig. 2 may be started with the ratios specified in the regulations and standards. The wall size recommendations given in Fig. 2 are in the nature of a preliminary design guide taken into account in the trial-and-error method (ACI 318R-05 2005; TS 7994 1990).

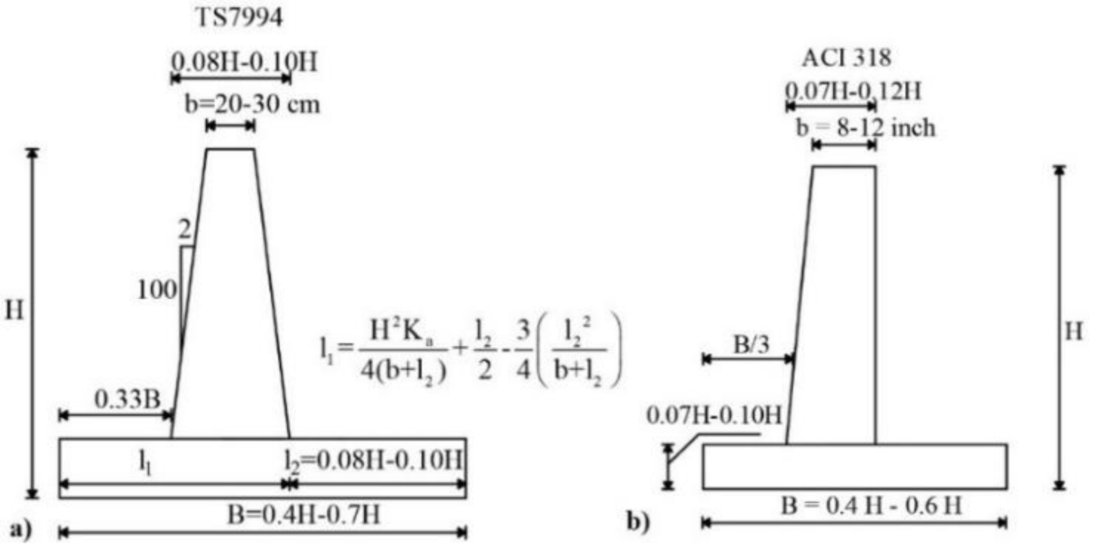

Fig. 2. Cantilever retaining wall preliminary design guides (Uray et al. 2021).

After pre-sizing the retaining wall design, investigations are made against sliding, overturning, bearing capacity, and slope stability, and the safety factors (F_s) are determined. In cases where the safety factor is not sufficient (F_s <1.50), the designer repeats the operations until it is satisfied (Das and Sivakugan 2017). The sliding behavior of the retaining wall, which is effective in determining the sliding safety factor considered in this study, is shown in Fig. 3.

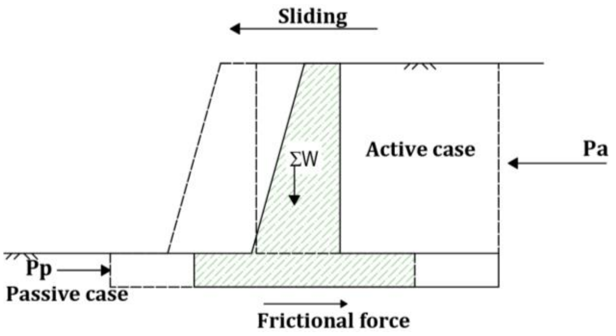

Fig. 3. Sliding behavior in retaining wall (Uray 2020).

The stability criteria of the cantilever retaining wall should be checked by considering soil properties obtained from the results of experiments and examinations conducted in the field and laboratory and design geometry. First of all, the lateral soil pressures affecting the retaining structure should be calculated by the designer with the theories in the literature. In this study, the lateral soil pressures considered in determining the sliding safety factor were determined according to the Rankine theory (Rankine 1857). In Rankine theory, calculations are made by regarding the stresses that occur when a soil medium reaches a state of plastic equilibrium. In elastic equilibrium, the soil is at rest; in the plastic case, it is in the case of active and passive thrust. For these three cases, the lateral soil pressures (σ_0, σ_a, σ_p) affecting the retaining structure can be calculated by multiplying the vertical stress (σ_v) with the coefficients of earth pressure at rest (K_0), active earth pressure (K_a), and passive earth pressure (K_p) given by Eqs. (1)–(3) (Orhan 2020), respectively.

$$K_0 = 1 - \sin\phi, \sigma_0 = K_0\sigma_v \quad \text{(at rest)} \tag{1}$$

$$K_a = \cos\beta \frac{\cos\beta - \sqrt{(\cos\beta)^2-(\cos\phi_{fs})^2}}{\cos\beta + \sqrt{(\cos\beta)^2-(\cos\phi_{fs})^2}}, \sigma_a = K_a\sigma_v \quad \text{(active case)} \quad (2)$$

$$K_p = \tan^2\left(45+\frac{\phi}{2}\right), \sigma_p = K_p\sigma_v \quad \text{(passive case)} \quad (3)$$

There, ϕ corresponds to the internal friction angle of the soil from which the horizontal soil thrust is determined, and β corresponds to the slope of the soil.

In this study, the design variables of cantilever retaining wall are top stem thickness (X_1), toe extension (X_2), bottom stem thickness (X_3), heel extension (X_4), base thickness (X_5) and they demonstrated in Fig. 4.

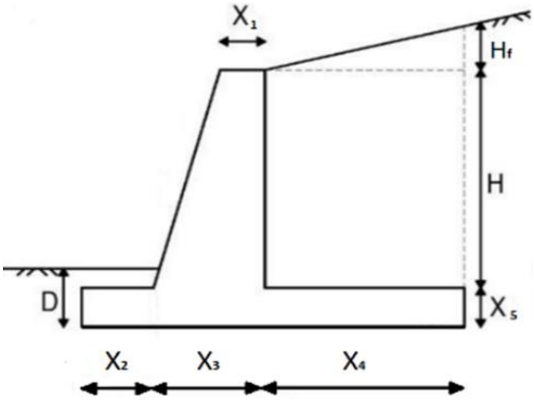

Fig. 4. Cantilever retaining wall design.

In the stability of the retaining wall against sliding, there is a balance between the sliding forces and the forces resisting sliding. A collapse scenario occurs when the forces resisting the slide are defeated. Since it is desired to stay on the safe side in the analysis, the ratio of the forces resisting slip (F_{sr}) given in Eq. (4) to the sliding forces (F_{sw}) given in Eq. (5) is defined as the sliding safety factor (F_{ss}) (Fig. 5). The mathematical expression of the sliding safety factor (F_{ss}) is given by Eq. (6).

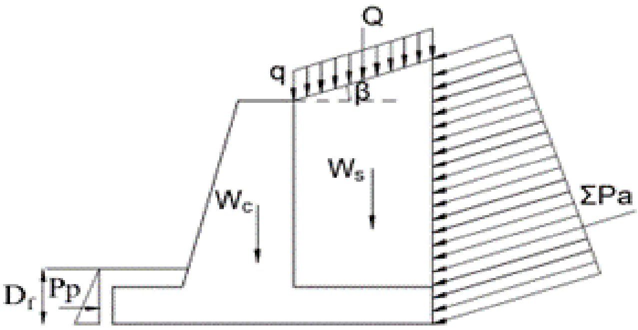

Fig. 5. Loads acting on the retaining wall.

$$F_{sr} = \Sigma V \tan\left(\frac{2}{3}\phi_{fb}\right) + \frac{2}{3}c_{fb}(X_2+X_3+X_4) + P_p$$

$$\Sigma V = W_c + W_s + Q + \Sigma P_{ay} \quad (4)$$

$$F_{sw} = \Sigma P_{ax} \quad (5)$$

$$F_{ss} = \frac{F_{sr}}{F_{sw}} \quad (F_{sw} = \Sigma P_{ax}) \quad (6)$$

W_c and W_s are the weight of the wall and the weight of the backfill soil above the heel extension, respectively. The active lateral soil force (P_a) formed by the soil supported by the retaining wall and the passive lateral soil force (P_p) formed along the base depth at the front of the wall are given by Eqs. (7) and (8), respectively.

$$P_a = 0.5K_a\gamma_{bs}(X_4\tan\beta + H + X_5)^2$$

$$P_{ax} = P_a\cos\beta, \ P_{ay} = P_a\sin\beta \quad (7)$$

$$P_p = 0.5K_p\gamma_{fs}{D_f}^2 + 2c_{fs}\sqrt{K_p}D_f \quad (8)$$

In this study, the sliding safety factors of the cantilever retaining wall was determined by taking into account the mathematical expressions and the geotechnical and slope properties of the soil environment given in Table 1.

Table 1. Cantilever bearing wall design parameters.

Parameter	Symbol	Value	Unit
Wall stem height	H	6	m
Surcharge load	q	0	kPa
Backfill slope	β	10	°
Internal friction angle of backfill soil and base soil	ϕ_{fs} and ϕ_{bs}	30	°
Unit weight of backfill soil and base soil	γ_{bs} and γ_{fs}	18	kN/m³
Friction angle between foundation base and soil	δ	2/3 ϕ_{bs}	°
Cohesion of backfill soil and base soil	c_{bs} and c_{fs}	0	kPa
Foundation depth	D_f	X_5	m

2.2. Fuzzy logic methods

In this section, data set, fuzzy logic methods, and evaluation criteria were given with implementation details of models for predicting the sliding safety factor (F_{ss}) of cantilever retaining wall. A data set consisting of 1024 different wall designs was prepared for the prediction of F_{ss} of the cantilever retaining wall. In the preparation of the data set, the design variables given in Fig. 4 were considered. 1024 (4^5) different wall designs (combinations) including all values of 5 design variables and 4 different values given in Table 2 were created. By utilizing safety factor dataset of these designs, the sliding safety factors were predicted by fuzzy logic methods.

Table 2. Cantilever retaining wall design parameters.

X_1 (m)	X_2 (m)	X_3 (m)	X_4 (m)	X_5 (m)
0.30	0.50	0.30	0.50	0.50
0.35	1.50	0.35	1.50	0.75
0.40	2.50	0.40	2.50	1.00
0.45	3.50	0.45	3.50	1.25

In prediction analysis, 1024 data set was randomly sorted and 922 (90%) and 102 (10%) of them were used as training and as test data, respectively. In the analyzes, two different iterations were tried and the effect of iteration on the modeling was also examined. The iterations used are ten (10) and one hundred (100). Looking at the correlation relationship between the inputs and F_{ss}; it is seen that they are 0.031 with X_1, 0.179 with X_2, 0.405 with X_3, 0.980 with X_4, and 0.005 with X_5.

Root Mean Square Error (*RMSE*), Mean Absolute Error (*MAE*) and Coefficient of Determination (R^2) were used as evaluation criteria. *RMSE*, *MAE*, and R^2 evaluation criteria are given in Eqs. (9)–(11), respectively.

$$RMSE = \sqrt{\frac{1}{N}\sum_{i=1}^{N}\left(F_{ss_e} - F_{ss_o}\right)^2} \tag{9}$$

$$MAE = \frac{1}{N}\sum_{i=1}^{N}\left|F_{ss_e} - F_{ss_o}\right| \tag{10}$$

$$R^2 = 1 - \frac{\sum_{i=1}^{N}\left(\sum F_{ss_o} - F_{ss_e}\right)^2}{\sum_{i=1}^{N}\left(\sum F_{ss_o} - \bar{F}_{ss_e}\right)^2} \tag{11}$$

In formulas, F_{ss_o}, F_{ss_e}, and N correspond to the observed F_{ss} value, pedicted F_{ss} value, and the number of data, respectively.

In Fig. 6, the implementation of ANFIS-GP and ANFIS-SC models for predicting F_{ss} are demonstrated.

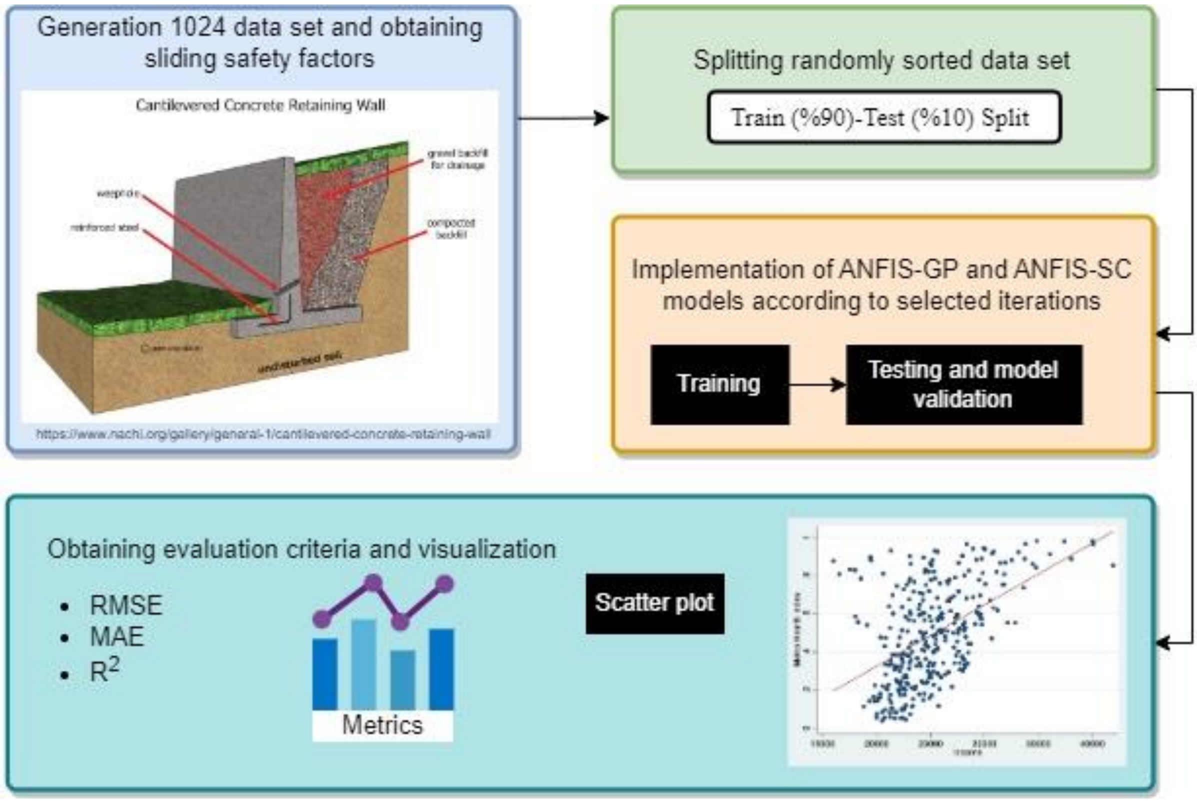

Fig. 6. Fuzzy logic based prediction of retaining wall stability.

Table 3 contains the inputs used in the study and the corresponding datasets.

Table 3. Inputs and datasets used in the study.

Inputs	Data Sets
1 input	X_1
2 input	$X_1 + X_2$
3 input	$X_1 + X_2 + X_3$
4 input	$X_1 + X_2 + X_3 + X_4$
5 input	$X_1 + X_2 + X_3 + X_4 + X_5$

2.2.1. Grid partition (GP)

When the GP fuzzy inference system is desired to be used, the learning of the model is basically based on the grid partitioning method. The Grid Partition method divides the data set into rectangular sub-areas, called grids, according to the previously determined number and types of membership functions to be used. In the subspace, each input is divided into membership functions of identical shape. The system creates fuzzy rules based on input-output training, optimizing data providing fast learning processes and computation time. When using this model; Membership functions of all antecedent variables can be defined. The basic logic of the system is to create rules by calculating all combinations of membership functions for the input variables to be used in the model to be created (Benmouiza and Cheknane 2019; Fattahi 2016; Hekim and Orhan 2011; Kaya 2018).

2.2.2. Substructive clustering (SC)

SC is applied when there is no clear idea about the number of centers for the distribution of data. It is one of the fuzzy clustering methods. It is similar to Mountain Clustering proposed by Yager and Filev (1994). However, since the grid is not used, the number of possible cluster centers depends only on the number of data, not on the dimensionality or distribution of the data (Yager and Filey 1994). The data point with the largest number of close neighbors is chosen as the cluster center. It positions other data points accordingly, where each point is a potential cluster center based on its own characteristics. It continues like this until the end. In this method, which is a good approach especially since it is independent of the initial condition, cluster centers are not determined except for data points. Therefore, the detected cluster centers may not be suitable for every data space (Fattahi 2016; Hekim and Orhan 2011; Kaya 2018; Priyono et al. 2005).

3. Findings and Discussion

Tables 4 and 5 show the test results of the models performed for 10 and 100 iterations using the GP and SC methods. In Figs. 7–10, the scatter plots prepared for each input set in 10 and 100 iterations of the GP and SC methods are given. Charts show observations and predictions of test data. In addition, the regression line and equation of the best-performing model in the form of *y=ax+b* and the coefficient of determination are given in the figures.

Table 4. Test results using 10 iterations.

Criteria	Algorithm	Inputs (10 iteration, test)					
		1 input	2 input	3 input	4 input	5 input	Avr.
RMSE	GP	0.324	0.319	0.321	0.016	0.004	0.197
	SC	0.324	0.322	0.331	0.017	0.001	0.199
	Avr.	0.324	0.320	0.326	0.016	0.002	0.198
MAE	GP	0.289	0.286	0.287	0.011	0.004	0.175
	SC	0.289	0.289	0.298	0.011	0.002	0.178
	Avr.	0.289	0.287	0.292	0.011	0.003	0.177
R^2	GP	0.001	0.026	0.015	0.998	0.999	0.408
	SC	0.007	0.011	0.002	0.997	0.999	0.403
	Avr.	0.004	0.018	0.009	0.997	0.999	0.406

Table 5. Test results using 100 iterations.

Criteria	Algorithm	Inputs (100 iteration, test)					
		1 input	2 input	3 input	4 input	5 input	Avr.
RMSE	GP	0.324	0.319	0.322	0.016	0.003	0.197
	SC	0.324	0.323	0.333	0.018	0.003	0.200
	Avr.	0.324	0.321	0.327	0.017	0.003	0.198
MAE	GP	0.289	0.287	0.289	0.011	0.002	0.175
	SC	0.289	0.290	0.299	0.012	0.002	0.178
	Avr.	0.289	0.288	0.294	0.011	0.002	0.177
R^2	GP	0.001	0.025	0.012	0.998	0.999	0.407
	SC	0.007	0.007	0.004	0.997	0.999	0.403
	Avr.	0.004	0.016	0.008	0.997	0.999	0.405

In the study conducted by Uray et al. (2019b), prediction models that provide sliding, overturning, and slope stability safety factors by using Multilayer Artificial Neural Networks, Generalized Regression Artificial Neural Networks, and Radial Based Artificial Neural Networks were submitted. According to the study, the model developed with Artificial Neural Networks can be used reliably in predictions of safety factors of the cantilever retaining wall. On the other hand, the prediction models of sliding, overturning, and slope stability safety factors were obtained by utilizing machine learning algorithms for cantilever retaining walls and creating a mathematical model based on regression that provides to calculation of the safety factors (Seyhan 2021). Looking at the results; observed that the correlation coefficient value is quite close to one. Thus, it has been revealed that the obtained mathematical model can be an important and practical solution for finding the value of safety factors in retaining structures.

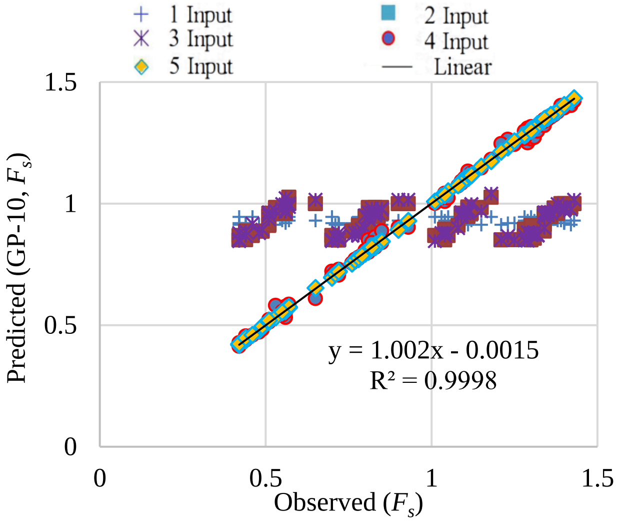

Fig. 7. Scatter plot for 10 iterations of the GP method.

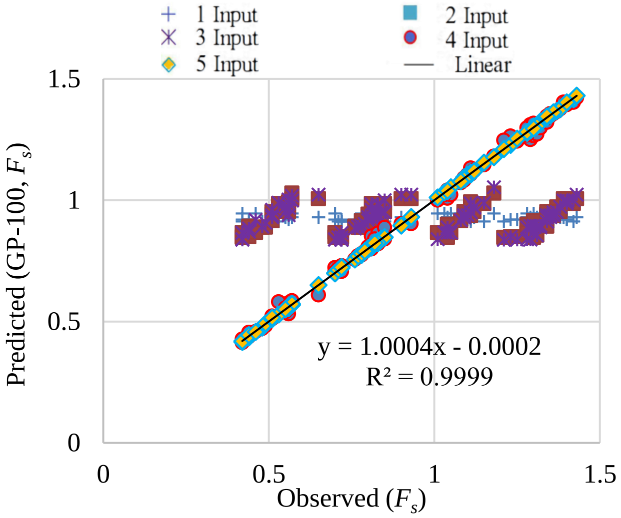

Fig. 8. Scatter plot for 100 iterations of the GP method.

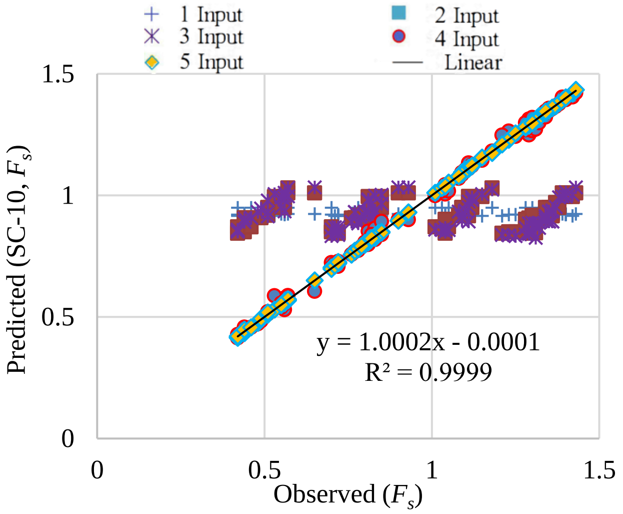

Fig. 9. Scatter plot for 10 iterations of SC method.

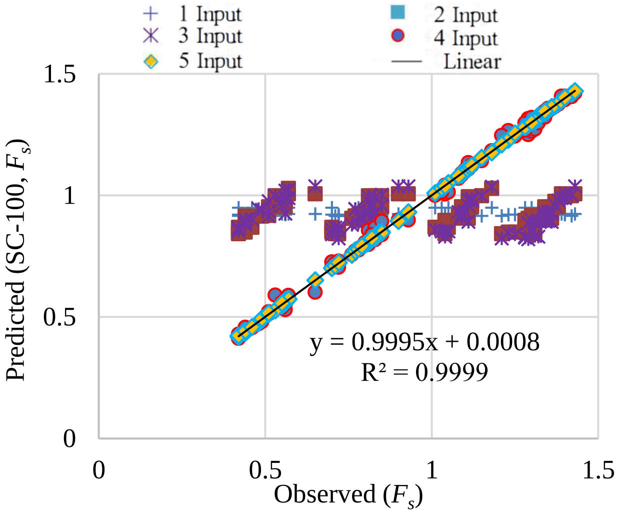

Fig. 10. Scatter plot of SC method for 100 iterations.

4. Conclusions

In this study, the prediction of retaining wall stability control was investigated using an adaptive network-based fuzzy inference system including ANFIS-GP and ANFIS-SC. In the study; A data set containing 1024 (4^5) different wall designs was created by considering four wall dimensions including stem thickness (X_1), toe extension (X_2), bottom stem thickness (X_3), heel extension (X_4), base thickness (X_5). Randomly selected 90% of these data were used in the training phase and the remaining 10% were used in the testing phase. In addition, two models were created by changing the number of iterations to 10 and 100. Models were compared using three different error criteria (*RMSE*, *MAE*, and R^2). When the results are examined;

- Since the best result is for ANFIS-SC with *MAE*= 0.002 *RMSE*=0.001, R^2= 0.999 for 10 iterations and 5 inputs, the ANFIS-SC method is more prosperous than the ANFIS-GP method in predicting safety factors.
- It has been determined that the errors are further reduced by including the 4th and 5th inputs in the models.
- It has been observed that the performance values obtained in the 1st, 2nd, and 3rd input sets of both methods are quite low (errors are high and the coefficient of determination is close to zero) and the predictions do not represent the observed values.
- The relationship between the input parameters employed in the models and the predicted sliding safety factors is consistent with the modeling performance. In other words, it was determined that the errors were less in the inputs with a high correlation coefficient.

- It has been inferred that the model with 100 iterations takes longer in different iteration applications and gives predictions with fewer errors.
- As a result, in this study, the sliding safety factors predicted by considering 1024 different wall designs were used and the success of the fuzzy logic methods in prediction was compared.
- When the evaluation criteria obtained are examined, it has been shown that fuzzy logic-based prediction methods can be used robustly and effectively in complex engineering design problems.

Author Contributions

All of the authors made substantial contributions to conception and design, or acquisition of data, or analysis and interpretation of data; were involved in drafting the manuscript or revising it critically for important intellectual content; and gave final approval of the version to be published.

Acknowledgements

The abstract of this study was presented at the symposium titled "1st International Conference on Applied Engineering and Natural Sciences".

Funding

The authors received no financial support for the research, authorship, and/or publication of this manuscript.

Conflict of Interest

The authors declared no potential conflicts of interest with respect to the research, authorship, and/or publication of this manuscript.

Data Availability

The datasets created and/or analyzed during the current study are not publicly available, but are available from the corresponding author upon reasonable request.

REFERENCES

ACI 318R-05 (2005). Building Code Requirements for Structural Concrete and commentary. American Concrete Institute, Farmington Hills, Mich.

Arama ZA, Kayabekir AE, Bekdaş G, Geem ZW (2020). CO2 and cost optimization of reinforced concrete cantilever soldier piles: A parametric study with harmony search algorithm. *Sustainability (Switzerland)*, 12(15), 7–10.

Arslan Ö, Keskin I, Ateş A (2018). Farklı deprem yüklerinin betonarme konsol bir istinat duvarının maliyetine etkisinin analizi. *Anadolu Üniversitesi Bilim ve Teknoloji Dergisi - B Teorik Bilimler*, 6, 28–35.

Başakın EE, Ekmekcioğlu Ö, Çıtakoğlu H, Özger M (2022). A new insight to the wind speed forecasting: robust multi-stage ensemble soft computing approach based on pre-processing uncertainty assessment. *Neural Computing and Applications,* 34, 783–812.

Benmouiza K, Cheknane A (2019). Clustered ANFIS network using fuzzy c-means, subtractive clustering, and grid partitioning for hourly solar radiation forecasting. *Theoretical and Applied Climatology,* 137(1–2), 31–43.

Binici E, Öztürk Ş (2019). Konsol istinat duvar tasarımı üzerine parametrik bir çalışma. *Iğdır Üniversitesi Fen Bilimleri Enstitüsü Dergisi,* 9(1), 203–210.

Citakoglu H, Cobaner M, Haktanir T, Kisi O (2014). Estimation of monthly mean reference evapotranspiration in Turkey. *Water Resources Management,* 28, 99-113.

Çıtakoğlu H, Coşkun, Ö (2021). Dalgacık dönüşüm modelli yapay zekâ teknikleri kullanılarak Orta Anadolu Bölge istasyonlarının yağış tahmini. *Harran Üniversitesi Mühendislik Dergisi,* 6(1), 39-54.

Dağdeviren U, Kaymak, B (2018). Investigation of parameters affecting optimum cost design of reinforced concrete retaining walls using artificial bee colony algorithm. *Journal of the Faculty of Engineering and Architecture of Gazi University,* 33(1), 239–253.

Das BM, Sivakugan N (2017). Principles of Foundation Engineering (9th Edition). Cengage Learning. Retrieved from http://thuvienso.hau.edu.vn:8888/dspace/handle/hau/5215

Fattahi H (2016). Indirect estimation of deformation modulus of an in situ rock mass: an ANFIS model based on grid partitioning, fuzzy c-means clustering and subtractive clustering. *Geosciences Journal,* 20(5), 681–690.

Gandomi AH, Kashani AR, Roke DA, Mousavi M (2015). Optimization of retaining wall design using recent swarm intelligence techniques. *Engineering Structures,* 103, 72–84.

Gokkus U, Yildirim MS, Yilmazoglu A (2018). Prediction of concrete and steel materials contained by cantilever retaining wall by modeling the artificial neural networks. *Journal of Soft Computing in Civil Engineering,* 2(4), 47-61.

Hekim M, Orhan, U (2011). Bulanık c-means kümeleme yöntemine çıkarımlı yaklaşım. *İTÜ Mühendislik Dergisi,* 10–1(356), 11–17.

Kaya H (2018). Akciğer hastalıkları teşhisinde sınıflandırma ve bulanık mantık yöntemlerinin uygulanması. *M.Sc. thesis,* Ankara University, Ankara.

Sağlamer A (1985). Derin kazıların sorunları ve destekleme sistemleri. *Derin Kazılar ve İksa Metodları Sempozyumu*. Boğaziçi University, İstanbul.

Manjunath K, Gowda K, Prasad, GE (2012). Optimization of cantilever earth retaining wall using artificial neural network. *Proceedings of National Conference on Innovations in Civil Engineering*.

Mishra P, Samui P, Mahmoudi E (2021). Probabilistic design of retaining wall using machine learning methods. *Applied Sciences,* 11(12), 5411.

Mustafa R, Samui P, Kumari S (2022). Reliability analysis of gravity retaining wall using hybrid anfis. *Infrastructures,* 7(9), 121.

Orhan M (2020). Geoteknik Mühendisliği ve Temel İnşaatı - I. Gazi University Publications, Ankara.

Önalp A, Arel E (2012). Geoteknik mühendisliğinde yapay sinir ağı uygulamaları ve bir örnek: Zemin profilinin tahmin edilmesi. *İTÜ Dergisi/d,* 10(4).

Priyono A, Ridwan M, Alias AJ, Atiq R, Rahmat OK, Hassan A, Ali, M (2005). Generation of fuzzy rules with subtractive clustering. *Jurnal Teknologi,* 43(1), 143–153.

Rankine W (1857). Earth Pressure Theory. Phil. Trans. of the Royal Soc.

Seyhan Ş (2021). Dayanma duvarlarında makine öğrenmesi ile güvenlik sayısı tahmini. *M.Sc. thesis*, KTO Karatay University, Konya.

Shahin MA, Jaksa MB, Maier HR (2009). Recent advances and future challenges for artificial neural systems in geotechnical engineering applications. *Advances in Artificial Neural Systems,* 2009.

TS 7994 (1990). Zemin Dayanma Yapıları; Sınıflandırma, Özellikleri ve Projelendirme Esasları, Turkish Standards Institute, Ankara.

Uray E, Carbas S, Erkan IH, Tan O (2019a). Parametric investigation for discrete optimal design of a cantilever retaining wall. *Challenge Journal of Structural Mechanics,* 5(3), 108-120.

Uray E, Demir V, Keskin A, Tan Ö (2019b). Use of artificial neural networks in stability control of cantilever retaining walls. *International Civil Engineering and Architecture Conference 2019*, Trabzon.

Uray E (2020). Dayanma Yapılarının Sezgisel Yöntemler Kullanılarak Optimum Tasarımı. *Ph.D.* thesis, Konya Technical University, Konya.

Uray E, Tan Ö, Çarbaş S, Erkan H (2021). Metaheuristics-based pre-design guide for cantilever retaining walls. *Teknik Dergi,* 32(4), 10967-10993.

Uray E, Carbas S, Geem ZW, Kim S (2022). Parameters optimization of Taguchi method integrated hybrid harmony search algorithm for engineering design problems. *Mathematics 2022,* 10(3), 327.

Yager RR, Filev DP (1994). Generation of fuzzy rules by mountain clustering. *Journal of Intelligent & Fuzzy Systems: Applications in Engineering and Technology,* 2(3), 209–219.

Yepes V, Alcala J, Perea C, González-Vidosa, F (2008). A parametric study of optimum earth-retaining walls by simulated annealing. *Engineering Structures,* 30(3), 821–830.

CHALLENGE JOURNAL OF STRUCTURAL MECHANICS 9 (4) (2023) 153–162

Research Article

On the evaluation of lateral-torsional buckling of web-tapered cantilevers with doubly symmetric I-section

Tolga Yılmaz [a,*], Mustafa Sertçelik [a], Hasan Selim Şengel [b]

[a] *Department of Civil Engineering, Konya Technical University, 42250 Konya, Türkiye*
[b] *Department of Civil Engineering, Eskişehir Osmangazi University, 26040 Eskişehir, Türkiye*

ABSTRACT

Recently, structural engineers have tended to design stronger and lighter structures due to economic reasons, technical developments in computer-aided design, and improvements in manufacturing. The demand for designing stronger and lighter structures has led to the compulsory considering structural efficiency and stability loss at the design level. Lateral-torsional buckling (LTB) is a major stability loss for web-tapered cantilevers with doubly symmetric I-section, which are aesthetic and structurally efficient. The elastic LTB loads of these cantilevers should be calculated at the design level since the LTB may happen before bending stress reaches yield. Studies related to the LTB of cantilevers are rare and require numerical solutions since the LTB mode shape of cantilevers is complex compared to simply supported beams. The present study introduces an analytical procedure based on the energy method for calculating elastic LTB of web-tapered cantilevers with doubly-symmetric I-section in two different forms. The analytical model considers different transverse load types, positions of loads, and web tapering degrees. The analytical solutions were validated with one-dimensional finite element analysis using a beam element. Excellent accordance between results was demonstrated. The general LTB behavior of web-tapered cantilevers with doubly symmetric I-section was clarified with detailed comments based on results obtained from the presented analytical model.

ARTICLE INFO

Article history:
Received 22 August 2023
Revised 10 November 2023
Accepted 1 December 2023

Keywords:
Lateral-torsional buckling
Web-tapered cantilevers
Finite element analysis
Analytical method

1. Introduction

Steel web-tapered cantilevers with I-section are very popular structural members by means of aesthetic features and light weights. A good optimization could be achieved by tapering their web along the cantilever length considering the variation of bending moment. In other words, web height is maximum at fixed support, and it decreases towards to free end since the bending moment is lowered too. However, a web-tapered cantilever bending about its major axis may buckle out of a plane by deflecting laterally and twisting for a level of the applied transverse load. This stability loss is called lateral-torsional buckling (LTB), and the critical load level where buckling occurs is elastic LTB load (Yilmaz 2023). Fig. 1 depicts the LTB of a cantilever. The elastic LTB load of beams, beam-columns, and cantilevers subjected to uniform bending can be calculated by solving related differential equations; however, analytical solutions may be very complex or include infinite series when moment distributions vary along the length of the structural member and/or structural member has support conditions differ from simple support (Yilmaz and Kirac 2017; Yilmaz et al. 2017, 2019; Yilmaz 2023). At this point, numerical methods such as finite differences (Ozbasaran 2013; Ozbasaran 2014; Assasi and Roeder 1985) and finite integral (Anderson and Trahair 1972; Kitipornchai et al. 1984) were utilized for the calculation of the elastic LTB load of cantilevers. Based on the finite element solutions performed, Xiao et al. (2023) derived practical equations to calculate the elastic LTB load of doubly symmetric cantilevers for essential load cases.

---

* *Corresponding author*. Tel.: +90-332-205-1500 ; Fax: +90-332-241-0635 ; E-mail address: tyilmaz@ktun.edu.tr (T. Yılmaz)

ISSN: 2149-8024 / DOI: https://doi.org/10.20528/cjsmec.2023.04.004

Nomenclature

A_i , B_i	The amplitudes of the buckled mode shape
b_f	Top and bottom flanges' width
C	Center of gravity
$C_w(z)$	The warping constant
$d(z)$	Heights of cross-section
E	Young's modulus
G	Shear modulus
$h(z)$	Heights of web
$h_0(z)$	The distance between flange centers
h_i	The height of the web at the fixed end
H_p	Vertical distance between the shear center and load application points for the point load
H_q	Vertical distance between the shear center and load application points for the distributed load
$I_y(z)$	The moment of inertia belonging to the weak axis
$J(z)$	Torsional constant
$M_x(z)$	The bending moment about the major axis
P	Point load
q	Distributed load
S	Shear center
t_f	Top and bottom flanges' thickness
u	Lateral displacement of the shear center
U	The strain energy stored in the cantilever
v	Vertical displacement of the shear center
V	The work done by the external transverse forces
V_M	Additional work done by the end moment acting on shear center
Π	The total potential energy of the cantilever
φ	Torsion rotation of the shear center
Φ_L	The free-end rotation
Φ_p	Torsional rotation at the application point of the point load

The energy method, which is based on the equality between the additional strain energy stored when LTB occurs and the additional work done by the applied forces, is a favorable approach to evaluating elastic LTB of steel structural members. To determine elastic LTB load with this method, a buckled shape that represents the actual mode shape and provides kinematic boundary conditions is substituted in the total potential equation belonging to the slightly buckled position (Yilmaz 2023; Trahair 1993). While closed-form equations for beam and beam-columns could be established using the energy method with basic mode shapes, it is hard or commonly impossible to generate equations for cantilevers due to their complex mode shape (Yilmaz 2023). The energy method was used to calculate the elastic LTB of beams, beam-columns, and castellated beams (Mohri et al. 2008; Kim et al. 2016; Torkamani and Roberts 2009; Yilmaz et al. 2017; Ozbasaran 2019; Saoula et al. 2021; Bresser et al. 2020; Belaid et al. 2018; Pham 2022). Furthermore, the LTB load of the beams with mono-symmetric I-sections (Yilmaz and Kirac 2017; Yilmaz et al. 2019; Mohri et al. 2003; Mohri et al. 2013; Aydin et al. 2015; Mohammadi et al. 2016), the beams with various cross sections such as C, Z and box (Cheng et al. 2013; Saoula et al. 2016; Zhang and Tong 2016), and cantilevers (Wang and Kitipornchai 1986; Ozbasaran et al. 2015; Andrade et al. 2007; Aydin et al. 2013; Zhang and Tong 2008; Zhang et al. 2016; Yilmaz 2023) were evaluated utilizing the energy method.

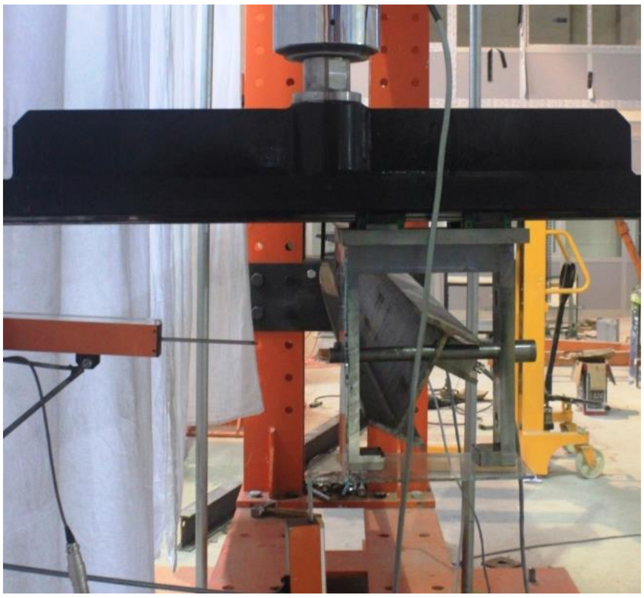

Fig. 1. The LTB of a cantilever.

Experimentally and analytical investigation on the stability of web or flange tapering beams with doubly symmetric and mono-symmetric I-sections were presented in studies by Kitipornchai and Trahair (1972) and Kitipornchai and Trahair (1975). Trahair (2017) developed a treatment based on the finite element method for calculating the LTB of tapered beam-columns, which is subjected to various load types and has different boundary conditions. Benyamina et al. (2013) developed a formula for LTB of web-tapered beams with doubly symmetric I-section. The LTB of beams with arbitrary cross-sections was studied by Asgarian et al. (2013). The LTB of the beams, of which flanges and web simultaneously tapered, was investigated by the study of Kus (2015). Trinh et al. (2023) introduced an approximate expression to evaluate the critical moment of simply supported I-section beams whose height changes. Osmani and Meftah (2018) presented a study focused on the LTB of symmetric beam-columns considering shear deformations. Yuan et al. (2013) studied the LTB of T-section cantilevers. The LTB of web-tapered mono-symmetric I-section cantilevers were examined by Andrade et al. (2007) and Andrade and Camotim (2005). In these comprehensive analytical studies, pre-buckling effects have been included in the energy method, and numerical LTB examples for beams and cantilevers subjected to point load were presented. It should be emphasized that elastic LTB load must be calculated with the above-mentioned methods and considered in design since LTB may occur before the bending stress of the cross-section's extreme fibre comes to yield.

The literature review conducted reveals that there is no comprehensive study related to the LTB of cantilevers with doubly-symmetric I-section exposed to different load cases by considering their positions along the cross-section. The primary motivation of the present study is to establish an analytical procedure based on the energy method, which is easily programmable with mathematical software, to determine the elastic LTB load of web-tapered cantilevers with doubly-symmetric I-section for six load cases and three loading positions which are top and bottom flange and shear center loadings. The analytical results were compared to one-dimensional finite element analysis (1D-FEA) using LTBeamN software. In light of the results of numerical examples, slenderness and tapering effects were interpreted, and explanations were presented. The study will contribute to understanding the uncharted LTB behaviour of web-tapered symmetric I-section cantilevers with detailed interpretations as well as the analytical procedure that enables the calculation of critical LTB load for the design of steel members.

2. Analytical Procedure

In the present study, the analytical model has been developed for web-tapered cantilevers with symmetric I-section, which have two different tapering forms illustrated in Fig. 2. In the first of two tapering forms, depicted in Fig. 2(a), web tapering has been provided by the obliquity of the bottom flange while the top flange is parallel to the cantilever's longitudinal z-axis. In the second form, illustrated in Fig. 2(b), web tapering has been provided by the obliquity of both the top and bottom flanges. In the study, cantilevers with the first tapering form will be named Cantilever Type 1 ($C1$), and Cantilever Type 2 ($C2$) will be used for the cantilevers with the second tapering form. Before the LTB occurs, the cantilever bends about its major axis under the effects of transverse loads, and then the cantilever buckles by deflecting laterally and twisting, shown in Fig. 2(c), when the magnitude of the loads reaches the elastic critical LTB load.

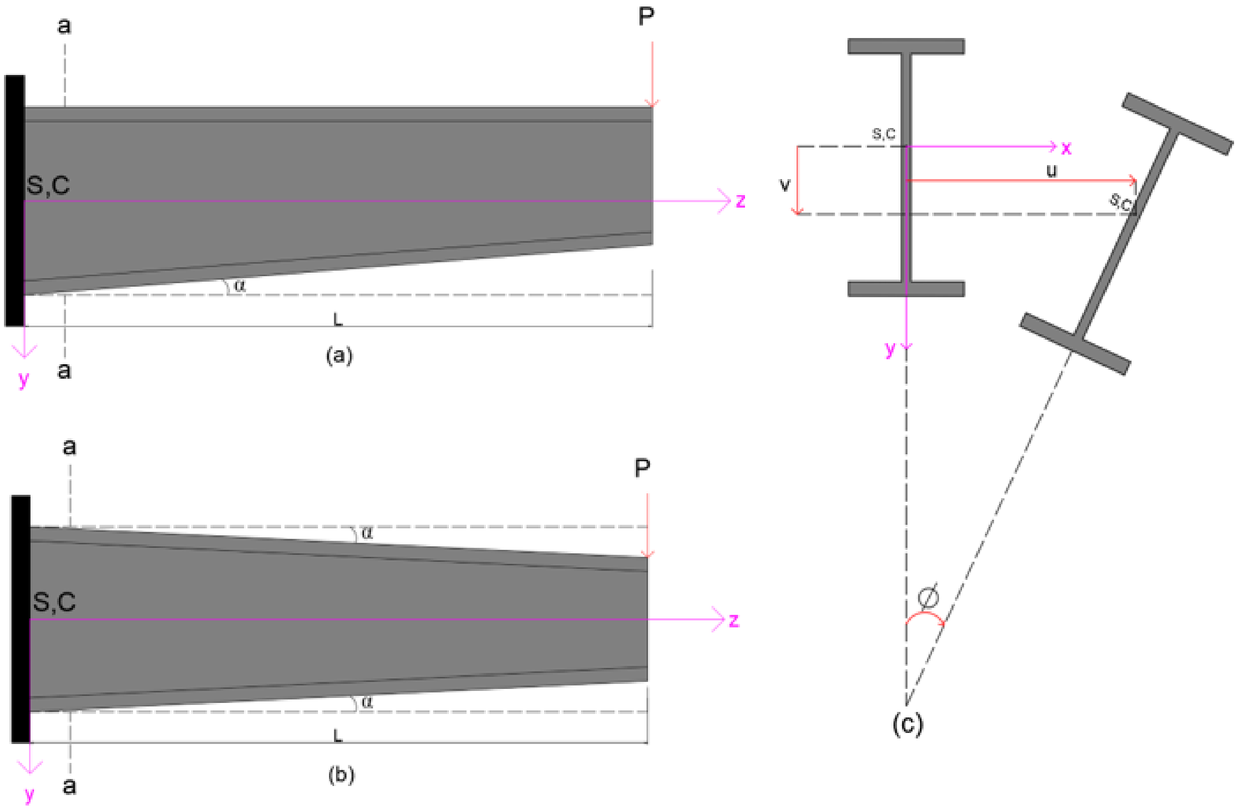

Fig. 2. The LTB of web-tapered cantilevers.

In Fig. 2(a), α and L are the tapering angle and the cantilever length, respectively. Fig. 2(c) illustrates the a-a section of the web-tapered cantilevers. In Fig. 2, while the S and C denote the shear center and the center of gravity, respectively, the lateral and vertical displacements and the torsional rotation of the shear center were given with u, v, and φ, respectively. Fig. 3 shows the cross-section dimensions of a web-tapered cantilever with a doubly symmetric I-section. In Fig. 3, while the top and bottom flange width is shown with b_f, the t_f denotes the top and bottom flanges' thickness. The d and h are heights of cross-section and web, respectively.

These two dimensions depend on the distance to the fixed end in the z-axis since h decreases with tapering. The height (h) can be expressed for the $C1$ and $C2$ cantilevers as given in Eqs. (1) and (2), respectively.

$$h(z) = h_i - z * \tan(\alpha) \tag{1}$$

$$h(z) = h_i - 2 * z * \tan(\alpha) \tag{2}$$

where h_i refers to the height of the web at the fixed end. Therefore d becomes:

$$d(z) = h(z) + 2 * t_f \tag{3}$$

The warping constant $C_w(z)$, torsional constant $J(z)$, and the moment of inertia belonging to the weak axis

$I_y(z)$ are the main parameters which effective on the LTB. For a web-tapered cantilevers in Fig. 2, $C_w(z)$, $J(z)$, and $I_y(z)$ can be expressed as follows:

$$C_w(z) = \frac{h_0^2(z) b^3 t_f}{24} \tag{4}$$

$$J(z) = \frac{2bt_f{}^3 + h_0(z) t_w^3}{3} \tag{5}$$

$$I_y(z) = \frac{2b^3 t_f + h(z) t_w^3}{12} \tag{6}$$

where the $h_0(z)$ is the distance between flange centers and given as follows:

$$h_0(z) = d(z) - t_f = h(z) + t_f \tag{7}$$

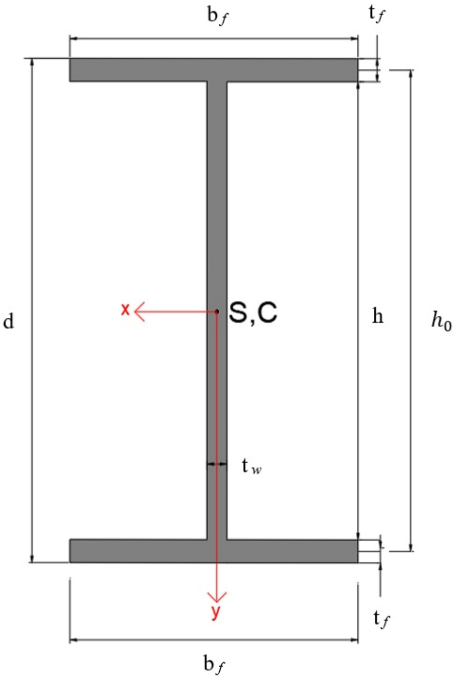

Fig. 3. The cross-section dimensions of the doubly symmetric I-section.

The strain energy stored in the cantilever due to lateral bending, warping, and torsion, respectively, can be written as follows (Yilmaz 2023; Yilmaz et al. 2019):

$$U = \frac{1}{2}\int_0^L EI_y(z)\left[\frac{d^2u(z)}{dz^2}\right]^2 dz + \frac{1}{2}\int_0^L EC_w(z)\left[\frac{d^2\phi(z)}{dz^2}\right]^2 dz + \frac{1}{2}\int_0^L GJ(z)\left[\frac{d\phi(z)}{dz}\right]^2 dz \tag{8}$$

where E and G are Young's modulus and shear modulus, respectively. The work done by the external transverse forces can be expressed as in Eq. (9) (Yilmaz 2023; Yilmaz et al. 2019):

$$V = \frac{1}{2}\int_0^L M_x(z)\left[2\phi(z)\left[\frac{d^2u(z)}{dz^2}\right]\right]dz + \frac{1}{2}\sum PH_p\phi_p^2 + \frac{1}{2}\int_0^L qH_q\phi(z)^2 dz + M\phi_L\left[\frac{du_L}{dz}\right] \tag{9}$$

where $M_x(z)$ implies the bending moment about the major axis. The works of point load P and distributed load q, acting out of the shear center, were taken place as second and third terms in Eq. (9). The source of these works is the variation of distance between the application point of loads and shear center during rotation of section. H_p and H_q denote the vertical distance between the shear center and load application points for P and q, respectively. H_p and H_q should be taken as positive when the load application point is below the shear center. The Φ_p shows torsional rotation at the application point of the point load.

Furthermore, an external moment acting on the shear center at the end of the cantilever generates additional work existing in the last term of Eq. (9). To understand this additional work V_M, end moment M is replaced with an equivalent force couple, which are in opposite directions and acts on flange centers. These forces displace relatively in longitudinal directions, leading to additional work when the cross-section rotates. V_M can be calculated by multiplying the magnitude of forces with their displacement in the longitudinal direction as follows (Yilmaz 2023):

$$V_M = 2\left[\frac{M}{h_0(L)}\right]\left[h_0(L)\frac{\phi_L}{2}\frac{du_L}{dz}\right] = M\phi_L\left[\frac{du_L}{dz}\right] \tag{10}$$

In Eq. (10), Φ_L is the free-end rotation. Eventually, the total potential energy ($\Pi=U+V$) of the cantilever can be expressed as in Eq. (11) by considering Vlassov's model. In this model, the cross-section is rigid in its plane, and the shear deformation belonging to the section's mean surface can be neglected (Yilmaz 2023).

$$\begin{aligned}\Pi = {} & \frac{1}{2}\int_0^L EI_y(z)\left[\frac{d^2u(z)}{dz^2}\right]^2 dz + \frac{1}{2}\int_0^L EC_w(z)\left[\frac{d^2\phi(z)}{dz^2}\right]^2 dz \\ & + \frac{1}{2}\int_0^L GJ(z)\left[\frac{d\phi(z)}{dz}\right]^2 dz + \frac{1}{2}\int_0^L M_x(z)\left[2\phi(z)\left[\frac{d^2u(z)}{dz^2}\right]\right]dz \\ & + \frac{1}{2}\sum PH_p\phi_p^2 + \frac{1}{2}\int_0^L qH_q\phi(z)^2 dz + M\phi_L\left[\frac{du_L}{dz}\right]\end{aligned} \tag{11}$$

The energy method predicates the equality of the strain energy stored due to the effect of LTB and the external forces' work. The energy method necessitates a buckled mode function representing the real buckled shape and providing boundary conditions that constrain deflection and/or rotations at supports. At fixed support of the cantilevers, all deflections and rotations are zero. Therefore, u, ϕ, du/dz, $d\phi/dz$ are taken as zero at fixed support. The u, ϕ, du/dz, $d\phi/dz$ are unconstrained at the free end. The cantilever mode shape can be defined as lateral deflection (u) and rotation angle (Φ), which belongs to the shear center. Bearing in mind above mentioned restrain conditions for cantilevers, the buckled mode function can be implied as in Eqs. (12) and (13). The amplitudes of the buckled mode shape were shown as A_i and B_i.

$$u(z) = \sum_{i=1}^{n} A_i\left(\frac{z}{L}\right)^{i+1} \tag{12}$$

$$\phi(z) = \sum_{i=1}^{n} B_i\left(\frac{z}{L}\right)^{i+1} \tag{13}$$

When buckled shape functions are substituted in Eq. (11), the total potential energy becomes as follows:

$$\Pi = U + V = f(A_1, A_2, A_3 \ldots, A_n, B_1, B_2, B_3 \ldots, B_n) \qquad (14)$$

The 2n variables of the total potential energy function are A_i and B_i. The LTB occurs when the total energy function reaches a stationary condition, which can be expressed with the following equations:

$$\frac{\partial \Pi}{\partial A_i} = 0 \quad \text{for } i = 1,2 \ldots n \qquad (15)$$

$$\frac{\partial \Pi}{\partial B_i} = 0 \quad \text{for } i = 1,2 \ldots n \qquad (16)$$

Eqs. (15) and (16) yield a system of 2n homogeneous linear equations, which can be expressed as follows:

$$[K]_{2nx2n}\,\{d\}_{2nx1} = \{0\}_{2nx1} \qquad (17)$$

where K is a coefficient matrix and $\{d\} = \{A_1, A_2, A_3 \ldots, A_n, B_1, B_2, B_3 \ldots, B_n\}^T$. Eq. (17) has been satisfied when the determinant of the K coefficient matrix equals zero.

$$\det\,[K]_{2nx2n} = 0 \qquad (18)$$

Eq. (18) yields a power series of order 2n, whose smallest feasible root gives the elastic LTB load or moment. The present analytical treatment can be easily programmed utilizing mathematical software such as Matlab, Mathematica, Mathcad, etc. The current analytical treatment can enable for calculation LTB load of both web-tapered cantilevers depicted in Fig. 2 under various load types considering their positions along the cross-sections.

3. Numerical Analysis

In the numerical analysis, based on the analytical model introduced, the elastic LTB loads of both web-tapered cantilevers $C1$ and $C2$ were calculated for six different load cases, presented in Fig. 4, and three loading positions, which are top flange, bottom flange, and shear center loadings. The end-moment loading was applied only on the shear center. The cantilevers' lengths and tapering angles were taken as variables to investigate the effects of the tapering and the slenderness on the LTB of $C1$ and $C2$ cantilevers. The section properties of cantilevers used in numerical analysis are given in Table 1. Names of cantilevers consist of four characters, the first two of which shows cantilever types $C1$ and $C2$, and the rest of two imply specimen number from $S1$ to $S11$. The d_e denotes the height of the cross-section at the free end. All dimensions in Table 1 are in units of mm. The tapering angles are in units of degree. The untapered cross-section was in dimensions of IPN-200, commonly used in structural practice. However, fillets were neglected, and flange thickness was assumed to be constant. The cantilever length was appropriate for the slender section assumption, considering crudely L/h>5. Similar cantilever lengths were used in previous works (Yilmaz 2023; Andrade and Camotim 2005). Previous studies argued that the energy method based on beam element assumption might not precisely reflect the LTB behavior of very compact sections and demonstrated the requirement for 3D finite element analysis (Yilmaz 2023; Andrade and Camotim 2005). Tapering angles were chosen to prevent excessive tapering at the free end according to the initial by considering manufacturing. Cantilever tapering was designed so that the cross-section height at the free end was not less than 50% of the height at the fixed end.

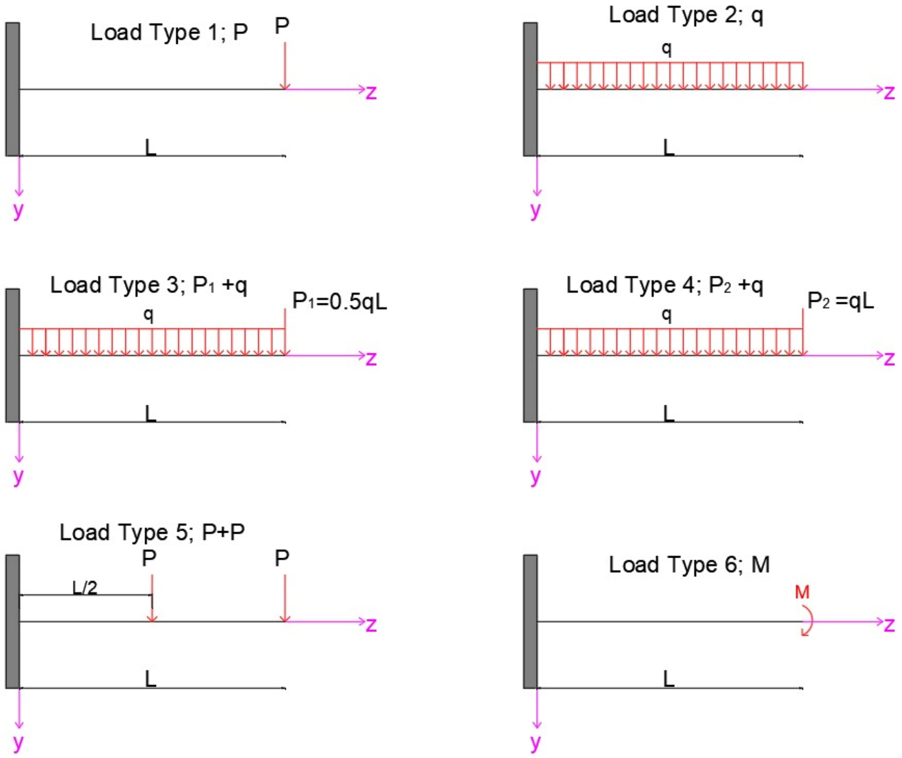

Fig. 4. The considered load types in the numeric analysis.

In the numerical analysis, the elastic modulus and Poisson's ratio were taken as $2\cdot10^5$ MPa and 0.3, respectively. All elastic buckling loads calculated via the presented analytical method were compared with the 1D finite element analysis (1D-FEA) using LTBeamN software (Centre Technique Industriel de la Construction Metallique 2015). LTBeamN software has been commonly used to solve elastic LTB problems in the literature (Yilmaz 2023; Kucukler and Gardner 2019; Yilmaz et al. 2017, 2019; Yilmaz and Kirac 2017; Kovac 2012). The software calculates the elastic LTB load analysis utilizing the beam elements that consider warping. LTBeamN allows users to define almost any common open section. Users can define sections using a pre-defined catalog or modifying dimensions for various cross-sections that are commonly used. Furthermore, sections may be defined by using their section properties that are effective in buckling. Users may change section height through its length to allow the analysis of haunched and tapered sections and assemble members from different upper and lower sections. The software provides flexibility for defining restraint conditions.

Table 1. The section properties of cantilevers used in the numerical analysis.

Variables	Sections	α	L	d	d_e	b_f	t_f	t_w
Tapering angles	C1S1	0	3000	200	200	90	11.3	7.5
	C1S2	0.955	3000	200	150	90	11.3	7.5
	C1S3	1.909	3000	200	100	90	11.3	7.5
	C2S4	0.477	3000	200	150	90	11.3	7.5
	C2S5	0.955	3000	200	100	90	11.3	7.5
Slenderness	C1S6	1.273	3000	200	133.34	90	11.3	7.5
	C1S7	1.273	3500	200	122.23	90	11.3	7.5
	C1S8	1.273	4000	200	111.12	90	11.3	7.5
	C2S9	0.637	3000	200	133.34	90	11.3	7.5
	C2S10	0.637	3500	200	122.23	90	11.3	7.5
	C2S11	0.637	4000	200	111.12	90	11.3	7.5

Restrain positions can be defined for any position both along the cross-section and length of the member. For each restraint, four different degrees of freedom can be defined. External and internal loading options can be used for loading structural members. In the external loading, concentrated and distributed loads can be added to the demanded positions along the cross-sections and length of the member. A bending diagram and axial load should be provided for buckling analysis in the internal loading. Besides, a self-weight of member may be added as an option. LTBeamN presents numerical results and graphical output to determine buckling loads and modes. Furthermore, the software has yielded compatible results with 3D finite element analysis (3D-FEA), where solid and shell elements are used (Yilmaz 2023; Yilmaz et al. 2017, 2019; Yilmaz and Kirac 2017). The numerical analysis results were presented in Tables 2-7 for six load cases respectively. These tables include elastic LTB loads of all cantilevers presented in Table 1 for top and bottom flange loadings and also shear center loadings. In the tables, AN and LT denote the elastic LTB loads obtained using the present analytical model and LTBeamN software. R implies the ratio of the analytical model results to the LTBeamN results.

Table 2. Load case 1, P_{cr} (kN).

	Top flange			Shear center			Bottom flange		
Cantilevers	AN	LT	R	AN	LT	R	AN	LT	R
C1S1	22.53	21.85	1.03	32.20	31.67	1.02	38.36	37.89	1.01
C1S2	24.41	23.69	1.03	31.53	31.03	1.02	36.31	35.82	1.01
C1S3	26.34	25.84	1.02	30.87	30.49	1.01	34.19	33.81	1.01
C2S4	24.41	23.69	1.03	31.53	31.03	1.02	36.31	35.82	1.01
C2S5	26.34	25.84	1.02	30.87	30.50	1.01	34.19	33.81	1.01
C1S6	25.06	24.39	1.03	31.31	30.84	1.02	35.61	35.14	1.01
C1S7	18.54	18.11	1.02	21.79	21.44	1.02	24.16	23.81	1.01
C1S8	14.19	13.88	1.02	16.00	15.73	1.02	17.39	17.12	1.02
C2S9	25.06	24.39	1.03	31.31	30.84	1.02	35.61	35.15	1.01
C2S10	18.55	18.11	1.02	21.79	21.44	1.02	24.15	23.81	1.01
C2S11	14.19	13.88	1.02	16.00	15.73	1.02	17.39	17.12	1.02

Table 3. Load case 2, q_{cr} (kN/m).

	Top flange			Shear center			Bottom flange		
Cantilevers	AN	LT	R	AN	LT	R	AN	LT	R
C1S1	24.78	24.11	1.03	39.86	39.23	1.02	53.75	53.12	1.01
C1S2	26.41	25.02	1.06	39.11	38.50	1.02	51.01	50.64	1.01
C1S3	28.20	26.17	1.08	38.36	37.87	1.01	48.16	48.26	1.00
C2S4	26.41	25.01	1.06	39.11	38.50	1.02	51.02	50.69	1.01
C2S5	28.21	26.16	1.08	38.36	37.88	1.01	48.16	48.36	1.00
C1S6	26.99	25.38	1.06	38.86	38.28	1.02	50.08	49.83	1.00
C1S7	17.08	16.11	1.06	22.86	22.49	1.02	28.34	28.21	1.00
C1S8	11.46	10.83	1.06	14.52	14.27	1.02	17.45	17.36	1.00
C2S9	26.99	25.36	1.06	38.85	38.29	1.01	50.07	49.91	1.00
C2S10	17.09	16.10	1.06	22.86	22.50	1.02	28.34	28.24	1.00
C2S11	11.46	10.82	1.06	14.52	14.27	1.02	17.44	17.38	1.00

When results presented in Tables 2-7 are examined, it has been found that the present analytical approach excellent matches with the 1D-FEA solutions performed with LTBeamN. Results demonstrated that the present analytical approach has been successful in capturing the effects of tapering level and slenderness on the LTB of web-tapered cantilevers. The average difference between analytical and numerical results is only 2%, and the maximum difference very rarely reaches 8% for compact sections where the energy method exhibits slightly worst performance on evaluation of the LTB since it bases on a beam element assumption. As slenderness increases, the beam element assumption becomes more valid; consequently, the energy method yields better accordant buckling loads with the FEA results. Similar tendencies were observed in previous studies (Yilmaz 2023; Yilmaz et al. 2019; Yilmaz and Kirac 2017).

It should be noted here that for short cantilevers, a more exact evaluation of the LTB may be achieved with 3D-FEA with shell element instead of the energy method based on 1D frame element assumption since the remarkable web and/or flange distortion or a localized web buckling phenomenon taking place near the application point of load is not captured with the 1D frame element assumption (Yilmaz 2023; Andrade et al. 2007; Ozbasaran et al. 2015).

It should be remembered that, as mentioned above, choosing a proper buckling mode shape reflecting the actual buckling mode is critical to the performance of the energy method. In the analytical calculations, sixth-order functions were used in Eqs. (12) and (13); in other words, n=5 was taken. With the increase of n, the difference between analytical and numerical results may be lowered. However, it must not be remembered that higher-order functions considerably increase computational time.

Table 4. Load case 3, $q_{cr}+0.5q_{cr}\cdot L$ (kN/m).

	Top flange			Shear center			Bottom flange		
Cantilevers	AN	LT	R	AN	LT	R	AN	LT	R
C1S1	9.53	9.26	1.03	14.18	13.95	1.02	17.90	17.68	1.01
C1S2	10.25	9.86	1.04	13.90	13.68	1.02	16.93	16.78	1.01
C1S3	11.01	10.57	1.04	13.61	13.45	1.01	15.93	15.91	1.00
C2S4	10.25	9.86	1.04	13.90	13.68	1.02	16.93	16.79	1.01
C2S5	11.01	10.57	1.04	13.61	13.45	1.01	15.93	15.93	1.00
C1S6	10.50	10.09	1.04	13.80	13.60	1.01	16.60	16.49	1.01
C1S7	6.65	6.41	1.04	8.19	8.06	1.02	9.54	9.47	1.01
C1S8	4.45	4.30	1.04	5.24	5.15	1.02	5.95	5.90	1.01
C2S9	10.50	10.09	1.04	13.80	13.60	1.01	16.60	16.49	1.01
C2S10	6.65	6.40	1.04	8.19	8.06	1.02	9.54	9.48	1.01
C2S11	4.45	4.29	1.04	5.24	5.15	1.02	5.95	5.91	1.01

Table 5. Load case 4, $q_{cr}+q_{cr}\cdot L$ (kN/m).

	Top flange			Shear center			Bottom flange		
Cantilevers	AN	LT	R	AN	LT	R	AN	LT	R
C1S1	5.85	5.68	1.03	8.56	8.42	1.02	10.58	10.45	1.01
C1S2	6.31	6.09	1.04	8.38	8.25	1.02	10.00	9.90	1.01
C1S3	6.78	6.57	1.03	8.21	8.11	1.01	9.41	9.37	1.00
C2S4	6.30	6.09	1.04	8.38	8.25	1.02	10.01	9.91	1.01
C2S5	6.78	6.57	1.03	8.21	8.11	1.01	9.41	9.38	1.00
C1S6	6.46	6.24	1.04	8.33	8.20	1.02	9.81	9.72	1.01
C1S7	4.09	3.97	1.03	4.95	4.87	1.02	5.66	5.61	1.01
C1S8	2.74	2.66	1.03	3.17	3.12	1.02	3.55	3.51	1.01
C2S9	6.46	6.24	1.04	8.33	8.20	1.01	9.81	9.73	1.01
C2S10	4.09	3.97	1.03	4.95	4.87	1.02	5.66	5.61	1.01
C2S11	2.74	2.66	1.03	3.17	3.12	1.02	3.55	3.51	1.01

Another critical finding revealing the general LTB behavior of web-tapered cantilevers, obtained from the numerical study, is that increases in tapering level, or other words, the tapering angles, have led to a decrease in elastic LTB loads for all load cases applied to the shear center and bottom flange. However, when transverse loads are acted on top flanges of web-tapered cantilevers, the LTB loads have increased with the increase of tapering. This unexpected result, less material providing more strength, can be explained by two opposite effects due to the increase in tapering. The first of these effects is the decrease in stiffness due to the rise in tapering. This effect causes a reduction in buckling load, as expected. The second effect stems from the decline in the distance between the application point of the transverse load and the shear center when tapering increases. In contrast to the first effect, this effect leads to a rise in buckling load. Consequently, since the second effect is more dominant, the elastic LTB load has increased when the load is applied to the top flange with the increase in tapering. It can be explicitly observed that these two effects tend to decrease buckling load with the increase of tapering when transverse loads are applied to the bottom flange. Therefore, for bottom flange loading, the increase in tapering cause a decrease in the LTB loads.

Table 6. Load case 5, $P_{cr}+P_{cr}$ (kN).

	Top flange			Shear center			Bottom flange		
Cantilevers	AN	LT	R	AN	LT	R	AN	LT	R
C1S1	19.25	18.68	1.03	29.00	28.51	1.02	37.38	36.90	1.01
C1S2	20.72	20.13	1.03	28.44	27.96	1.02	35.36	34.87	1.01
C1S3	22.23	21.81	1.02	27.87	27.51	1.01	33.26	32.86	1.01
C2S4	20.72	20.13	1.03	28.44	27.96	1.02	35.37	34.87	1.01
C2S5	22.23	21.81	1.02	27.87	27.51	1.01	33.26	32.87	1.01
C1S6	21.22	20.68	1.03	28.25	27.81	1.02	34.67	34.20	1.01
C1S7	15.67	15.08	1.04	19.56	19.29	1.01	23.19	23.11	1.00
C1S8	11.99	11.71	1.02	14.30	14.04	1.02	16.49	16.22	1.02
C2S9	21.22	20.68	1.03	28.25	27.81	1.02	34.67	34.20	1.01
C2S10	15.67	15.30	1.02	19.56	19.23	1.02	23.19	22.84	1.02
C2S11	11.99	11.72	1.02	14.30	14.04	1.02	16.49	16.23	1.02

4. Conclusions

The present study has established an analytical treatment to evaluate the lateral-torsional buckling behavior of web-tapered doubly symmetric I-section cantilevers. In the scope of the study, two different forms of cantilevers, of which web tapering is created by the obliquity of only the bottom flanges and both top and bottom flanges.

The analytical model considers the variation of moment distribution, the position of transverse load along the cross-section, and the tapering level. Thus, cantilevers were investigated under six load cases and three loading positions in numerical analysis. The LTB loads obtained by the analytical method were compared to 1D finite element analysis.

It has been found that there is only, on average, a 1%

difference between numerical and analytical LTB loads. An increase in tapering caused a decrease in the LTB loads when the transverse load was applied to the bottom flange and shear center; however, the opposite tendency occurred for top flange loadings. The increase in tapering has brought along two opposite effects, which are effective on the LTB of web-tapered cantilevers subjected to top flange loading. The first is a decrease in stiffness, which cause a reduction in buckling loads, and the second is a decrease in the distance between the application point of loads and the shear center, leading to an increase in buckling load. For top flange loading, since the second effect is more dominant, the LTB loads have increased when tapering increased.

Table 7. Load case 6, M_{cr} (kN·m).

	Shear center		
Cantilevers	AN	LT	R
C1S1	26.62	25.96	1.03
C1S2	25.91	24.93	1.04
C1S3	25.18	24.15	1.04
C2S4	25.91	24.93	1.04
C2S5	25.18	24.16	1.04
C1S6	25.67	24.64	1.04
C1S7	21.70	20.88	1.04
C1S8	18.77	18.11	1.04
C2S9	25.67	24.64	1.04
C2S10	21.70	20.88	1.04
C2S11	18.77	18.11	1.04

Author Contributions

All of the authors made substantial contributions to conception and design, or acquisition of data, or analysis and interpretation of data; were involved in drafting the manuscript or revising it critically for important intellectual content; and gave final approval of the version to be published.

Acknowledgements

The present study results are based on a section that exists in the Master of Science thesis, which Mustafa Sertçelik has been being prepared at the Graduate Education Institute, Konya Technical University. Dr. Tolga Yılmaz is a supervisor of the thesis.

Funding

The authors received no financial support for the research, authorship, and/or publication of this manuscript.

Conflict of Interest

The authors declared no potential conflicts of interest with respect to the research, authorship, and/or publication of this manuscript.

Data Availability

The datasets created and/or analyzed during the current study are not publicly available, but are available from the corresponding author upon reasonable request.

REFERENCES

Anderson JM, Trahair NS (1972). Stability of monosymmetric beams and cantilevers. *Journal of Structural Division*, 98(ST1), 269-86.

Andrade A, Camotim D (2005). Lateral–torsional buckling of singly symmetric tapered beams: Theory and applications. *Journal of Engineering Mechanics*, 131, 586–597.

Andrade A, Camotim D, Dinis PB (2007). Lateral-torsional buckling of singly symmetric web-tapered thin-walled I-beams: 1D model vs. shell FEA. *Computers and Structures*, 85, 1343–1359.

Andrade A, Camotim D, Providência e Costa P (2007). On the evaluation of elastic critical moments in doubly and singly symmetric I section cantilevers. *Journal of Constructional Steel Research*, 63, 894-908.

Asgarian B, Soltani M, Mohri, F (2013). Lateral-torsional buckling of tapered thin-walled beams with arbitrary cross-sections. *Thin-Walled Structures*, 62, 96-108.

Assadi M, Roeder CW (1985). Stability of continuously restrained cantilevers. *Journal of Engineering Mechanics*, 111(12), 1440–1456.

Aydin, R, Gunaydin A, Kirac N (2015). On the evaluation of critical lateral buckling loads of prismatic steel beams. *Steel and Composite Structures*, 18(3), 603-621.

Aydin R, Ozbasaran H, Kirac N, Gunaydin A (2013). Lateral torsional buckling of double angle and tee cantilevers: A parametric study. *Proceedings of the Fourteenth International Conference on Civil, Structural and Environmental Engineering Computing*, Civil-Comp Press, Stirlingshire, Scotland.

Belaid T, Ammari F, Adman R. (2018). Influence of load position on critical lateral torsional buckling moment of laterally restrained beam at tense flange. *Asian Journal of Civil Engineering*, 19, 839–48.

Benyamina AB, Meftah, S., Mohri F, Daya EM (2013). Analytical solutions attempt for lateral torsional buckling of doubly symmetric web-tapered I-beams. *Thin-Walled Structures*, 56, 1207-1219.

Bresser D, Ravenshorst GJP, Hoogenboom PCJ. (2020). General formulation of equivalent moment factor for elastic lateral torsional buckling of slender rectangular sections and I-sections. *Engineering Structures*, 207, 110-230.

Kim B, Li L, Edmonds A (2016). Analytical solutions of lateral-torsional buckling of castellated beams. *International Journal of Structural Stability and Dynamics*, 16, 155044.

Kitipornchai S, Dux PF, Richter NJ (1984). Buckling and bracing of cantilevers. *Journal of the Structural Division*, 110 (9), 2250-2262.

Kitipornchai S, Trahair NS (1972). Elastic stability of tapered I-beams. *Journal of the Structural Division*, 98(ST3), 713–728

Kitipornchai S, Trahair NS (1975). Elastic behaviour of tapered monosymmetric I-beams. *Journal of the Structural Division*, 101(ST8), 1661–1678

Kováč M. (2012). Lateral-torsional buckling of web-tapered I-beams 1D and 3D FEM approach. *Procedia Engineering*, 40, 217–22.

Kucukler M, Gardner L. (2019). Design of web-tapered steel beams against lateral-torsional buckling through a stiffness reduction method. *Engineering Structures*, 190, 246–61.

Kus J (2015). Lateral-torsional buckling steel beams with simultaneously tapered flanges and web. *Steel and Composite Structures*, 19(4), 897–916.

LTBeamN (2015). Centre Technique Industriel de la Construction Metallique.

Mohammadi E, Hosseini SS, Rohanimanesh SM (2016). Elastic lateral-torsional buckling strength and torsional bracing stiffness requirement for monosymmetric I-beams. *Thin-Walled Structures*, 104, 116-125.

Mohri F, Bouzerira C, Potier-Ferry M (2008). Lateral buckling of thin-walled beam-column elements under combined axial and bending loads. *Thin-Walled Structures*, 46(3), 290–302.

Mohri F, Brouki A, Roth JC (2003). Theoretical and Numerical Stability Analyses of Unrestrained, Mono-Symmetric Thin-Walled Beams. *Journal of Constructional Steel Research*, 59(1), 63-90.

Mohri F, Damil N, Potier-Ferry M (2013). Buckling and lateral buckling interaction in thin-walled beam-column elements with mono-symmetric cross sections. *Applied Mathematical Modelling*, 37(5), 3526–3540.

Osmani A, Meftah SA (2018). Lateral buckling of tapered thin walled bi-symmetric beams under combined axial and bending loads with shear deformations allowed. *Engineering Structures*, 165, 76–87.

Ozbasaran H (2013). Finite differences approach for calculating elastic lateral torsional buckling moment of cantilever I sections. *Anadolu University Journal of Science and Technology- A- Applied Science and Engineering*, (2), 143–152.

Ozbasaran H (2014). A parametric study on the evaluation of lateral torsional buckling of European IPE and IPN beams. *World Academy of Science, Engineering and Technology International Journal of Civil and Environmental Engineering*, 8(7), 783-788.

Ozbasaran H (2019). Convergence of the Rayleigh–Ritz Method for buckling analysis of arbitrarily configured I-section beam–columns. *Archive of Applied Mechanics*, 89, 2397–414.

Ozbasaran H, Aydın R, Dogan M (2015). An alternative design procedure for lateral-torsional buckling of cantilever I-beams. *Thin-Walled Structures*, 90, 235-242.

Pham PV (2022). An innovated theory and closed form solutions for the elastic lateral torsional buckling analysis of steel beams/columns strengthened with symmetrically balanced GFRP laminates. *Engineering Structures*, 256, 114-046.

Saoula A, Meftah SA, Mohri F, Daya EM (2016). Lateral buckling of box beam elements under combined axial and bending loads. *Journal of Constructional Steel Research*, 116, 141-155.

Saoula A, Selim MM, Meftah SA, Benyamina AB, Tounsi A (2021). Simplified analytical method for lateral torsional buckling assessment of RHS beams with web openings. *Structures*, 34, 2848–60.

Torkamani MAM, Roberts ER (2009). Energy equations for elastic flexural-torsional buckling analysis of plane structures. *Thin-Walled Structures*, 47(4), 463-473.

Trahair NS (1993). Flexural-Torsional Buckling of Structures. CRC Press, London, UK.

Trahair NS (2017). Lateral buckling of tapered members. *Engineering Structures*, 151, 518–26.

Trinh DK, Nguyen DH, Bui HC, Nguyen MT (2023). Lateral torsional buckling of I-section simply supported beams with stepped height. *Steel Construction*, 16, 1-6.

Wang CM, Kitipornchai S (1986). On stability of monosymmetric cantilevers. *Engineering Structures*, 8, 168-180.

Xiao G, Ho S, Papangelis JP (2023). Semi analytical solutions for flexural-torsional buckling of thin-walled cantilever beams with doubly symmetric cross-sections. *Structural Engineering and Mechanics*, 87, 541-554.

Yilmaz T (2023). Rapid evaluation of lateral-torsional buckling of European standard I-section cantilevers. *Mechanics Based Design of Structures and Machines*.

Yilmaz T, Kirac N (2017). Analytical and parametric investigations on lateral torsional buckling of European IPE and IPN beams. *International Journal of Steel Structures*, 17, 695–709.

Yilmaz T, Kirac N, Anil Ö (2019). An alternative evaluation of the LTB behavior of mono-symmetric beam-columns. *Steel and Composite Structures*, 30, 471–81.

Yilmaz, T, Kirac N, Kilic T (2017). Lateral-torsional buckling of european wide flange I-section beams. *Proceedings of the 2nd World Congress on Civil Structural and Environmental Engineering* (*CSEE'17*).

Yuan W, Kim B, Chen C (2013). Lateral-torsional buckling of steel web tapered tee-section cantilevers, *Journal of Constructional Steel Research*, 87, 31–37.

Zhang L, Tong GS (2016). Lateral buckling of simply supported C- and Z-section purlins with top flange horizontally restrained. *Thin-Walled Structures*, 99, 155-167.

Zhang L, Tong GS (2008). Elastic flexural-torsional buckling of thin-walled cantilevers. *Thin-Walled Struct*ures, 46, 27–37.

Zhang WF, Liu YC, Hou GL, Chen KS, Ji J, Deng Y (2016). Lateral-torsional buckling analysis of cantilever beam with tip lateral elastic brace under uniform and concentrated load. *International Journal of Steel Structures*, 16, 1161–73.